

UCLA

UCLA Previously Published Works

Title

PGC-1 α Controls Skeletal Stem Cell Fate and Bone-Fat Balance in Osteoporosis and Skeletal Aging by Inducing TAZ

Permalink

<https://escholarship.org/uc/item/89v8g9xj>

Journal

Cell Stem Cell, 23(2)

ISSN

1934-5909

Authors

Yu, Bo

Huo, Lihong

Liu, Yunsong

et al.

Publication Date

2018-08-01

DOI

10.1016/j.stem.2018.06.009

Peer reviewed



Published in final edited form as:

Cell Stem Cell. 2018 August 02; 23(2): 193–209.e5. doi:10.1016/j.stem.2018.06.009.

PGC-1 α Controls Skeletal Stem Cell Fate and Bone-Fat Balance in Osteoporosis and Skeletal Aging by Inducing TAZ

Bo Yu^{1,*}, Lihong Huo¹, Yunsong Liu², Peng Deng¹, John Szymanski¹, Jiong Li¹, Xianghang Luo³, Christine Hong⁴, Jiandie Lin⁵, and Cun-Yu Wang^{1,6,7,*}

¹Laboratory of Molecular Signaling, Division of Oral Biology and Medicine, School of Dentistry, University of California, Los Angeles, Los Angeles, CA 90095, USA

²Department of Prosthodontics, School of Stomatology, Peking University, Beijing 100081, China

³Department of Endocrinology, Endocrinology Research Center, Xiangya Hospital of Central South University, Changsha, Hunan 410008, People's Republic of China

⁴Division of Growth and Development, School of Dentistry, University of California, Los Angeles, Los Angeles, CA 90095, USA

⁵Life Sciences Institute, Department of Cell and Developmental Biology, University of Michigan, Ann Arbor, MI, USA

⁶Department of Bioengineering, Henry Samueli School of Engineering and Applied Science, Broad Stem Cell Research Center and Jonsson Comprehensive Cancer Center, University of California, Los Angeles, Los Angeles, CA 90095, USA

⁷Lead Contact

SUMMARY

Aberrant lineage specification of skeletal stem cells (SSCs) contributes to reduced bone mass and increased marrow adipose tissue (MAT) in osteoporosis and skeletal aging. Although master regulators of osteoblastic and adipogenic lineages have been identified, little is known about factors that are associated with MAT accumulation and osteoporotic bone loss. Here, we identify peroxisome-proliferator-activated receptor γ coactivator 1- α (PGC-1 α) as a critical switch of cell fate decisions whose expression decreases with aging in human and mouse SSCs. Loss of PGC-1 α promoted adipogenic differentiation of murine SSCs at the expense of osteoblastic differentiation. Deletion of PGC-1 α in SSCs impaired bone formation and indirectly promoted bone resorption while enhancing MAT accumulation. Conversely, induction of PGC-1 α attenuated osteoporotic bone loss and MAT accumulation. Mechanistically, PGC-1 α maintains bone and fat balance by

*Correspondence: boyu@dentistry.ucla.edu (B.Y.), cwang@dentistry.ucla.edu (C.-Y.W.).

AUTHOR CONTRIBUTIONS

B.Y., C.H., and C.-Y.W. conceived of this study. B.Y. and L.H. performed all main experiments and analyzed data. P.D., Y.L., J.S., and C.H. assisted B.Y. and L.H. with animal studies and histology. J. Li assisted B.Y. with ChIP assays. X.L. prepared human SSCs. J. Lin provided reagents and helped design experiments. B.Y. and C.-Y.W. wrote the paper.

DECLARATION OF INTERESTS

The authors declare no competing interests.

SUPPLEMENTAL INFORMATION

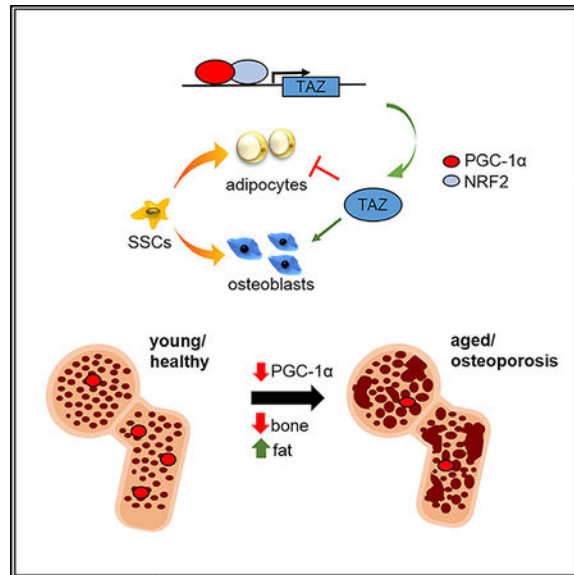
Supplemental Information includes seven figures and one table and can be found with this article online at <https://doi.org/10.1016/j.stem.2018.06.009>.

inducing TAZ. Our results suggest that PGC-1 α is a potentially important therapeutic target in the treatment of osteoporosis and skeletal aging.

In Brief

Yu et al. show that the metabolic regulator PGC-1 α regulates bone-fat balance in osteoporosis. Loss of PGC-1 α in SSCs impaired bone formation and promoted MAT accumulation. Mechanistically, PGC-1 α directly controlled SSC fate decision by inducing TAZ expression. Induction of PGC-1 α could attenuate bone loss and MAT accumulation in osteoporosis.

Graphical Abstract



INTRODUCTION

Skeletal stem cells (SSCs) are a subset of bone marrow stromal cells with the ability of self-renewal and multiple lineage potentials contributing to the osteoblast and adipocyte progenies in the adult bone marrow (Bianco et al., 2013; Bianco and Robey, 2015; Zhou et al., 2014). Recent lineage-tracing efforts further identify a shared reservoir of multipotent progenitors residing in the perivascular niche that can become unilaterally committed to either an osteogenic or adipogenic lineage (Ambrosi et al., 2017; Zhou et al., 2014). With the exception of certain animal strains or models (Ackert-Bicknell et al., 2009; Justesen et al., 2004), the commitment toward these lineages is classically considered to be inversely related, as the osteogenic differentiation of SSCs requires a coordinated inhibition of adipogenic differentiation (Kawai and Rosen, 2010; McCauley, 2010). Consistent with this reciprocal relationship, multiple cross-sectional human studies have also confirmed correlations between high marrow fat content, low bone density, and increased fracture risk, particularly in the context of osteoporosis and skeletal aging (Fazeli et al., 2013; Schwartz, 2015; Zaidi et al., 2012). Osteoporosis is the most common metabolic bone disease, posing a substantial public health burden in our aging population. In addition to the established

paradigm where osteoporosis is caused by an imbalance between osteoclasts and osteoblasts, emerging evidence suggests another pathogenic process involving aberrant lineage allocation of SSCs (Devlin and Rosen, 2015; Fan et al., 2017; Ye et al., 2012). Increased marrow adipose tissue (MAT) accumulation takes place at the expense of bone formation and in turn impairs osteogenic regeneration and hematopoiesis (Ambrosi et al., 2017). As the only tissue where bone and fat coexist in the same microenvironment, the bone marrow offers a unique window into the investigation of molecular events governing SSC lineage commitment.

The transcriptional control of cell fate decisions is strictly orchestrated by molecular signals and cues from the tissue microenvironment. During the last decade, several transcriptional factors associated with SSC fate commitment have been identified. For instance, while Runx2 and Osterix are master regulators of differentiation toward an osteogenic lineage, PPAR γ and CEBP $\alpha/\beta/\delta$ are considered essential for adipogenesis (Farmer, 2006). Molecular factors from the tissue microenvironment may further prime SSCs toward certain lineages and modulate the response of SSCs to lineage-specific stimulators (Gregory et al., 2005; Li et al., 2017). Aging or senescent SSCs may have a greater propensity to differentiate toward adipocytes than osteoblasts (Fan et al., 2017). Identifying these molecular switches is particularly useful when formulating strategies to counteract aberrant lineage allocations associated with pathological conditions such as osteoporosis and skeletal aging.

Originally discovered in brown fat to mediate adaptive thermogenesis, peroxisome-proliferator-activated receptor γ coactivator 1- α (PGC-1 α), encoded by *PPARGC1A*, is a master regulator of mitochondrial biogenesis and oxidative metabolism in skeletal muscle, liver, brain, and heart by serving as a critical transcriptional co-activator that regulates the expression of thermogenic genes (Puigserver et al., 1998; Lin et al., 2005). Dysregulated PGC-1 α has been associated with the pathogenesis of insulin resistance and cardiomyopathy (Arany et al., 2005). It is also a key player in mediating the defense against reactive oxygen species (ROS) production and inflammation in mitochondrial-rich cells (Balaban et al., 2005). Genetic studies using knockout mouse models have demonstrated that PGC-1 α is required for the induction of thermogenic genes, but not for brown fat differentiation (Uldry et al., 2006). PGC-1 α has been reported to prevent skeletal muscle aging and activate lipogenesis of muscle lipids (Gill et al., 2018). Interestingly, we found that the level of PGC-1 α was decreased with aging in bone tissues. Although PGC-1 α serves as a co-activator associated with the adipogenic master regulator PPAR γ , unexpectedly, we found that loss of PGC-1 α promotes adipogenic differentiation of SSCs at the expense of osteogenesis. The mesenchymal cell-specific deletion of PGC-1 α promotes bone loss and MAT accumulation in osteoporosis. In contrast, induction of PGC-1 α attenuates the adipogenic shift in osteoporosis and promotes bone formation.

RESULTS

Loss of PGC-1 α Potentiates Bone Loss and MAT Accumulation in Skeletal Aging

Skeletal aging represents an important scenario where decreased bone mass is met with increased MAT accumulation. Intriguingly, we found that while highly present in mouse bone marrow SSCs, the expression of *Ppargc1a* decreased significantly in 18-month-old

mice compared to 3-month-old mice (Figure 1A). On the other hand, the expression of *Pparg1a* did not change significantly in bone marrow monocytes and/or macrophages (Figure 1B). Immunohistochemical staining (IHC) and quantification of integral optical density (IOD) further confirmed that PGC-1 α expression was dramatically decreased in bone cells surrounding the trabecular bone and marrow cells of aged mice (Figure 1C). To examine if PGC-1 α was involved with skeletal aging, we utilized global *Pparg1a*^{-/-} (*Pgc1*^{-/-}) mice where PGC-1 α expression could not be detected in the bone cells surrounding the trabecular bone and in marrow cells (Figure 1D). The depletion of PGC-1 α mRNA in bone marrow cell extracts was also confirmed by RT-PCR (Figure 1E). Next, we examined whether PGC-1 α plays a role in age-related bone loss. Micro-computed tomography (μ CT) analysis of femurs revealed that 18-month-old *Pgc1a*^{+/+} mice lost ~40% of bone mineral density (BMD) and 50% of bone volume (BV/TV) compared to 3-month-old *Pgc1a*^{+/+} mice. While young *Pgc1a*^{-/-} mice and *Pgc1a*^{+/+} mice had comparable bone mass, 18-month-old *Pgc1a*^{-/-} mice lost ~58% of BMD and ~60% of BV/TV compared to their 3-month-old counterparts (Figure 1F). Meanwhile, 18-month-old *Pgc1a*^{+/+} mice had a greater trabecular number and less trabecular separation compared to age-matched *Pgc1a*^{-/-} mice (Figure S1A). Histomorphometric analysis showed that the osteoblast number (Ob.N) and osteoblast surface (Ob.S) were significantly lower in aged *Pgc1a*^{-/-} mice than in aged *Pgc1a*^{+/+} mice (Figure 1G). Consistent with the inhibition of osteoblast differentiation in aged *Pgc1a*^{-/-} mice, serum levels of osteocalcin (OCN), a marker for bone formation, were reduced by 67% in aged *Pgc1a*^{-/-} mice, which was significantly greater than the 50% reduction observed in *Pgc1a*^{+/+} mice (Figure 1H). Dynamic histomorphometry further confirmed that bone formation rate and mineral apposition were significantly inhibited in aged *Pgc1*^{-/-} mice compared to *Pgc1a*^{+/+} mice (Figures 1I and S1B). Of note, PGC-1 α depletion also led to a markedly greater number of osteoclasts in aged *Pgc1a*^{-/-} mice compared to their age-matched *Pgc1a*^{+/+} littermates, as evidenced by tartrate-resistant acid phosphatase (TRAP) staining and serum TRAP5b levels (Figures S1C–S1E). H&E staining of femurs confirmed that PGC-1 α depletion enhanced bone loss associated with aging. Surprisingly, we also noted marked changes in adipocyte accumulation (Figure 1J). Aged *Pgc1a*^{+/+} mice showed a significantly greater adipocyte number (81% increase) and adipocyte area (232% increase) compared to young *Pgc1a*^{+/+} mice. This aging-related MAT accumulation was significantly enhanced in *Pgc1a*^{-/-} mice (166% increase in adipocyte number and 732% increase in adipocyte area) (Figure 1K). This exacerbation of adipocyte accumulation in *Pgc1a*^{-/-} mice was confirmed by immunostaining for the adipocyte marker FABP4 with anti-FABP4 antibodies (Figure 1L). Cortical bone thickness was not significantly different between *Pgc1a*^{+/+} and *Pgc1a*^{-/-} mice at 18 months (Figure S1F), although the expression PGC-1 α also decreased with age (Figure S1G).

To verify the implications of aging on PGC-1 α expression in human skeletal tissues, we examined mRNA expression of *PPARGC1A* specifically in SSCs isolated from human bone marrow of young (age 20–40 years) and old (age 70–90 years) subjects. In both males and females, there was a >5-fold decrease in PGC-1 α expression in older marrow SSCs compared to younger SSCs (Figure 1M). Thus, PGC-1 α could influence the aging-induced shift in bone-fat balance by mediating SSC lineage decisions.

Depletion of PGC-1 α in Mesenchymal Cells Exacerbates Bone-Fat Imbalance in Osteoporosis

Since PGC-1 α expression in human SSCs decreased dramatically with age and global *Pgc1a*^{-/-} mice exhibited a reciprocal impact on osteoblast and adipocyte differentiation, we explored whether SSC lineage specification is intrinsically regulated by PGC-1 α . Paired related homeobox 1 (*Prx1*) is a transcriptional coactivator that is expressed during limb bud development, and *Prx1-Cre* has been widely used to delete genes in multipotent mesenchymal cells, including SSCs (Logan et al., 2002; Xiong et al., 2011). We conditionally deleted PGC-1 α in SSCs using *Prx1-Cre*. *Scal*⁺*CD29*⁺*CD45*⁻*CD11b*⁻ SSCs were isolated from the long bone marrow of *Prx1Cre;Pparg1a*^{fllox/fllox} (*Prx1;Pgc1a*^{fl/f}) and control *Prx1;Pgc1a*^{w/w} mice (Chang et al., 2013; Wang et al., 2014). Depletion of PGC-1 α mRNA levels in SSCs was confirmed via qRT-PCR (Figure 2A, left). Levels of PGC-1 α in bone marrow monocytes and/or macrophages were similar between *Prx1;Pgc1a*^{fl/f} mice and *Prx1;Pgc1a*^{w/w} mice, confirming specific depletion in SSCs (Figure 2A, right). Osteoporosis is a major metabolic bone disease in which bone loss is accompanied by MAT accumulation. Ovariectomy (OVX) is an established model used to simulate postmenopausal estrogen deficiency and induce osteoporotic bone loss. As such, we investigated if conditional depletion of PGC-1 α affected osteoporotic bone loss and MAT accumulation in mice following OVX. μ CT analysis indicated that *Prx1;Pgc1a*^{fl/f} mice did not have significant differences in bone mass compared to *Prx1;Pgc1a*^{w/w} mice in sham-operated groups. However, while ovariectomized *Prx1;Pgc1a*^{w/w} mice showed 45% lower BMD and 40% lower BV/TV compared to mice in the sham group, *Prx1;Pgc1a*^{fl/f} mice exhibited a significantly greater reduction in both bone density (60%) and bone volume (54%) after OVX (Figure 2B). Histomorphometric measurements showed that OVX caused an increase in osteoblast counts to compensate for increased bone resorption in *Prx1;Pgc1a*^{w/w} mice, but not in *Prx1;Pgc1a*^{fl/f} mice (Figure 2C). Measurement of serum OCN levels also confirmed that bone formation was less effective in *Prx1;Pgc1a*^{fl/f} mice after OVX than in *Prx1;Pgc1a*^{w/w} mice (Figure 2D). Dynamic histomorphometry showed that rates of bone formation and mineral apposition were significantly suppressed in *Prx1;Pgc1a*^{fl/f} mice after OVX (Figures 2E and S2A). Meanwhile, the adipocyte number and area were significantly greater in *Prx1;Pgc1a*^{fl/f} mice than in *Prx1;Pgc1a*^{w/w} mice after OVX, whereas no marked difference was observed in sham groups (Figures 2F–2H and S2H), suggesting that depletion of PGC-1 α in SSCs impaired bone formation and enhanced osteoporosis-induced MAT accumulation. To further evaluate the effect of PGC-1 α depletion on the formation of MAT, we performed μ CT analysis of osmium-tetroxide-stained lipids in mouse tibial bone marrow following OVX. Skeletal MAT shows region specificity whereby the proximal tibial adipocytes, termed regulated MAT (rMAT), are actively regulated by processes such as aging and temperature change, while constitutive MAT (cMAT) is constitutively present in the distal tibia (Scheller et al., 2015). Indeed, *Prx1;Pgc1a*^{fl/f} mice demonstrated a significantly enhanced increase in rMAT, but not in cMAT, after OVX in the proximal tibia compared to *Prx1;Pgc1a*^{w/w} mice (Figure 2I), affirming that depletion of PGC-1 α in SSCs enhanced marrow adiposity.

Leptin receptor (LepR) has recently been identified as a marker of SSCs attributing for a majority of the osteoblasts and adipocytes in adult bone marrow (Kfoury and Scadden, 2015;

Zhou et al., 2014). Lineage mapping showed that LepR⁺ cells are rare in embryonic bone marrow, but with increasing age, they contributed to greater percentage of osteoblasts and adipocytes in the adult bone marrow (Zhou et al., 2014). To further confirm our results, we also generated *LepRcre;Ppargc1a^{fl/fl}* (*LepR;Pgc1a^{fl/fl}*) mice. qRT-PCR verified the conditional depletion of *Ppargc1a* in SSCs, but not in bone marrow monocytes and/or macrophages (Figure 3A). Consistent with the conditional deletion of PGC-1 α in SSCs using *Prx1cre*, *LepR;Pgc1a^{fl/fl}* mice also displayed enhanced bone loss following OVX compared to control *LepR;Pgc1a^{w/w}* mice (58% versus 45% reduction in BMD; 68% versus 56% reduction in BV/TV) (Figures 3B). Osteoblast differentiation and function was markedly suppressed in *LepR;Pgc1a^{fl/fl}* mice after OVX (Figure 3C). Consistently, this inhibition was confirmed by serum OCN levels (Figure 3D). Dynamic histomorphometry showed a significant inhibition of bone formation in *LepR;Pgc1a^{fl/fl}* mice following OVX (Figures 3E and S3A). Moreover, OVX-induced rMAT accumulation was markedly greater in *LepR;Pgc1a^{fl/fl}* mice than in *LepR;Pgc1a^{w/w}* mice (Figures 3F–3I and S3D).

Because we observed a significant enhancement of osteoclast increase in aged *Pgc1a^{-/-}* mice, and because accelerated osteoclastic resorption is a critical contributor to OVX-induced bone loss, we also examined the impact of PGC-1 α depletion in SSCs on osteoclasts. Interestingly, while OVX induced osteoclast activation in *Prx1;Pgc1a^{w/w}* mice, osteoclast activation was further enhanced in *Prx1;Pgc1a^{fl/fl}* mice after OVX (Figures S2B–S2D). To further rule out the nonspecific effect, we also examined bone resorption in *LepR;Pgc1a^{fl/fl}* mice. Similarly, osteoclast activation upon OVX was significantly higher in *LepR;Pgc1a^{fl/fl}* mice than in *LepR;Pgc1a^{w/w}* mice (Figures S3B and S3C). Bone marrow monocytes and/or macrophages are osteoclast precursor cells. Since *Ppargc1a* was not deleted in both *Prx1;Pgc1a^{fl/fl}* mice and *LepR;Pgc1a^{fl/fl}* mice (Figures 2A and 3A), we hypothesized that loss of PGC1 α in SSCs and their progenies might indirectly affect osteoclast differentiation. It has long been known that the loss of PGC-1 α promotes inflammation and secretes pro-inflammatory cytokines in muscle, heart, and liver by activating nuclear factor-kappa B (NF- κ B) (Handschin and Spiegelman, 2008). Therefore, it is possible that loss of PGC-1 α in bone marrow stromal or mesenchymal cells enhances NF- κ B activation and the production of pro-inflammatory cytokines. Subsequently, these pro-inflammatory cytokines could enhance osteoclastogenesis and bone resorption induced by OVX. Therefore, we directly examined whether loss of PGC-1 α promoted NF- κ B activation in SSCs. Indeed, our luciferase assays showed that the deletion of PGC-1 α in SSCs significantly increased NF- κ B-dependent luciferase activity (Figure S4A). Rescue of PGC-1 α in *Pgc-1a^{-/-}* SSCs with adenoviruses expressing PGC-1 α (adPGC-1 α) significantly reduced NF- κ B-dependent luciferase activity (Figure S4B). Consistently, we found that depletion of PGC-1 α significantly enhanced the expression of the pro-inflammatory cytokine IL-6 (interleukin-6), a known NF- κ B target gene (Figure S4C). In contrast, overexpression of PGC-1 α in wild-type (WT) SSCs with adPGC-1 α suppressed IL-6 induction (Figure S4D), and restoration of PGC-1 α in *Pgc-1a^{-/-}* SSCs adPGC-1 α significantly reduced the expression of IL-6 compared to control *Pgc-1a^{-/-}* SSCs (Figure S4E). These results suggest that elevated expression of pro-inflammatory cytokines in *Pgc1a^{-/-}* SSCs enhances osteoclast formation and bone resorption upon OVX. Furthermore, we examined whether PGC-1 α modulated the local inflammatory microenvironment in the bone

marrow to achieve a paracrine effect on surrounding osteoclasts. As evidenced by immunostaining of the active form of the NF- κ B subunit p65 (Chang et al., 2009), NF- κ B activation in the bone lining cells and some bone marrow cells was significantly enhanced by PGC1 α depletion in *Prx1;Pgc1a^{f/f}* mice (Figures S2F and S2G).

Thus, our findings suggest that loss of PGC-1 α in bone marrow mesenchymal cells could increase NF- κ B-dependent expression of pro-inflammatory cytokines and subsequently enhance osteoclast activation induced by OVX.

PGC-1 α Intrinsically Controls SSC Fate Decisions

To confirm our *in vivo* findings and further delineate the role of PGC-1 α in SSC lineage decisions, we examined the effect of gain and loss of function of PGC-1 α on osteogenic and adipogenic differentiation of SSCs from bone marrow *in vitro*. SSCs derived from *Pgc1a^{-/-}* mice showed significantly less alkaline phosphatase (ALP) activity (Figure 4A) and mineralized nodule formation (Figure 4B) after 7 and 14 days of stimulation with osteogenic induction media, respectively. In contrast, overexpression of PGC-1 α by adPGC-1 α in SSCs significantly enhanced ALP activity and mineralized nodule formation (Figures 4C, 4D, S4F, and S4G). To further confirm our results, we also restored PGC-1 α expression in SSCs isolated from *Pgc1a^{-/-}* mice via adPGC-1 α (Figure 4C). Restoration of PGC-1 α in *Pgc1a^{-/-}* SSCs significantly increased ALP activity and mineralized nodule formation *in vitro* compared to *Pgc1a^{-/-}* SSCs expressing the empty vector (Figures 4D, S4F, and S4G). Consistently, overexpression of PGC-1 α in SSCs also enhanced the expression of key osteogenic marker genes, including *Runx2*, *Ibsp*, *Coll1a1*, and *Bglap* (Kalajzic et al., 2005; Chang et al., 2009). Restoration of PGC-1 α in *Pgc1a^{-/-}* SSCs significantly restored the expression of key osteogenic marker genes (Figure 4E).

On the other hand, depletion of PGC-1 α in SSCs significantly enhanced adipogenic differentiation, as evidenced by oil red O staining (Figure 4F). Overexpression of PGC-1 α in SSCs significantly inhibited adipogenic differentiation. Moreover, the restoration of PGC-1 α in *Pgc1a^{-/-}* SSCs potently reversed the increase in adipogenesis due to loss of PGC-1 α (Figure 4G). qRT-PCR confirmed that loss of PGC-1 α enhanced the expression of the key adipogenic marker genes *Pparg* and *Cd36* (Gregoire et al., 1998), while overexpression of PGC-1 α inhibited their expression (Figure 4H). Finally, restoration of PGC-1 α in *Pgc1a^{-/-}* SSCs significantly inhibited the expression of *Pparg* and *Cd36* compared to control *Pgc1a^{-/-}* SSCs.

We further validated the effect of PGC-1 α on lineage differentiation in human SSCs. Knockdown of human *PPARGC1A* via small interfering RNA (siRNA) in human SSCs resulted in significant inhibition of osteogenic differentiation (Figures S4H–S4K), as well as enhancement of adipogenic differentiation (Figures S4L and S4M). In contrast, overexpression of *PPARGC1A* via adenovirus in human SSCs enhanced osteogenic differentiation but inhibited adipogenesis (Figures S4N–S4S).

Depletion of PGC-1 α in Osteoblasts Exacerbates Osteoporotic Bone Loss, but Not MAT Accumulation

While PGC-1 α has intrinsic effects on SSCs, it may also be required for osteoblast function. However, if PGC-1 α controls SSC lineage specifications by inhibiting adipogenic differentiation, then the deletion of PGC-1 α in differentiated osteoblasts should not affect adipogenic differentiation. Moreover, if PGC-1 α in SSCs controls adipogenesis, then deletion of PGC-1 α in osteoblasts should not affect MAT accumulation in osteoporosis. To test these possibilities, we deleted PGC-1 α in osteoblasts *in vivo* using a 2.3-kb type 1 collagen promoter-driven Cre (2.3Col1-Cre). RT-PCR confirmed that we were able to delete PGC-1 α in osteoblasts of 2.3Col1-Cre;*Pgc1a*^{f/f} mice (2.3cre*Pgc1a*^{f/f}), but not other tissues (Figure 5A). μ CT analysis revealed that while control 2.3cre*Pgc1a*^{w/w} mice lost 35% of BMD and 45% of BV/TV 1 month following OVX, 2.3cre*Pgc1a*^{f/f} mice lost 53% of BMD and 61% of BV/TV (Figure 5B). Consistently, using toluidine blue staining, we found that depletion of PGC-1 α in osteoblasts resulted in a significant decrease in osteoblast counts (Figure 5C). Consistently, the bone formation rate (Figures 5D and S5A) and serum OCN level (Figure 5E) in 2.3cre*Pgc1a*^{f/f} mice were considerably lower after OVX compared to those in 2.3cre*Pgc1a*^{w/w} mice. Isolated calvarial preosteoblasts from *Pgc1a*^{-/-} mice also showed significantly reduced osteogenic differentiation potential compared to those from *Pgc1a*^{+/+} mice (Figures S5D and S5E).

However, while bone formation was significantly suppressed, there was no significant difference in the adipocyte number and area between 2.3cre*Pgc1a*^{f/f} and 2.3cre*Pgc1a*^{w/w} mice upon OVX (Figures 5F and 5G). μ CT analysis of rMAT and cMAT also revealed no significant difference between 2.3cre*Pgc1a*^{f/f} and 2.3cre*Pgc1a*^{w/w} mice after OVX (Figure 5H).

Induction of PGC-1 α Attenuates Bone-Fat Imbalance in Osteoporosis

Since loss of PGC-1 α promoted adipogenic differentiation at the expense of osteogenic differentiation and PGC-1 α decreased with aging in SSCs, we explored whether induction of PGC-1 α *in vivo* reversed the bone-fat imbalance observed in osteoporosis. We utilized a doxycycline-inducible *Ppargc1a* transgenic mouse by cross-mating Rosa26-rtTA mice with tetO-*Ppargc1a* mice (Russell et al., 2004) to generate Rosa26-rtTA;tetO-*Ppargc1a* (rtTA;tetO-*Pgc1a*) mice and control (wt;tetO-*Pgc1a*) mice. The *Ppargc1a* transgene was placed under the control of a tetracycline operator, which could be activated by doxycycline treatment and the reverse tetracycline-controlled transactivator (rtTA) that was constitutively expressed under the Rosa26 locus. Immunostaining of bone marrow confirmed the induction of PGC-1 α in rtTA;tetO-*Pgc1a* mice after doxycycline treatment (Figure 6A). We then performed OVX on rtTA;tetO-*Pgc1a* and wt;tetO-*Pgc1a* mice. μ CT analysis showed that OVX induced a significantly smaller loss of BMD (20% versus 38%) and BV/TV (25% versus 42%) in rtTA;tetO-*Pgc1a* mice than in wt;tetO-*Pgc1a* mice (Figures 6B and 6C). Morphometric analysis also indicated that induced PGC-1 α enhanced the increase in osteoblast surface (Ob.S/BS) after OVX (Figure 6D). The dynamic mineral deposition rate was significantly enhanced in rtTA;tetO-*Pgc1a* mice after OVX compared to wt;tetO-*Pgc1a* mice, while no significant difference was observed in the sham groups (Figures 6E and S6A). Serum analysis also confirmed that induced PGC-1 α expression promoted bone

formation following OVX (Figure 6F). Meanwhile, MAT accumulation following OVX was significantly suppressed in *rtTA;tetO-Pgc1a* mice compared to *wt;tetO-Pgc1a* mice, as evidenced by histomorphometric analysis (Figures 6G and 6H). FABP4 staining further confirmed that the induction of PGC-1 α inhibited adipogenesis induced by OVX (Figure 6I). Furthermore, μ CT analysis of marrow adiposity found that the induction of PGC-1 α in *rtTA;tetO-Pgc1a* mice significantly inhibited OVX-induced rMAT accumulation compared with *wt;tetO-Pgc1a* mice, while cMAT was not affected (Figure 6J).

Our results thus far indicate that PGC-1 α depletion in SSCs impacts lineage specification following OVX, while PGC-1 α may also play a role in the maturation and function of osteoblasts. In addition, PGC-1 α might regulate the expansion and maintenance of osteoblasts as well as adipocytes following OVX. To explore this possibility, we performed immunofluorescent staining (IF) of the proliferative marker Ki67 and the apoptotic marker active caspase-3 in perilipin (PLIN)-labeled adipocytes and OCN-labeled osteoblasts. Interestingly, while PGC-1 α depletion in *Prx1;Pgc1a^{fl/fl}* and *LepR;Pgc1a^{fl/fl}* mice significantly increased the total number of PLIN⁺ cells, the proportions of Ki67⁺ or active caspase-3⁺ cells in PLNP⁺ cells were not significantly different between control and conditional knockout mice (Figures S2I and S3F). Meanwhile, the proportions of Ki67⁺ or active caspase-3⁺ cells in OCN⁺ cells were also similar in both control and conditional knockout mice (Figures S2J and S3G). Similar observations were also made in *2.3crePgc1a^{fl/fl}* (Figure S5B and S5C) and *rtTA;tetO-Pgc1a* mice (Figures S6B and S6C). As such, PGC-1 α is unlikely to contribute to the expansion or maintenance of osteoblasts and adipocytes after OVX.

PGC-1 α Controls Bone-Fat Balance through TAZ

Oxidative stress accumulation is associated with bone loss in osteoporosis and skeletal aging (Manolagas, 2010; Wilson, 2014). Since PGC-1 α plays a key role in modulating oxidative stress in a variety of mitochondria-rich tissues (Balaban et al., 2005; St-Pierre et al., 2006), we hypothesized that the loss of PGC-1 α could increase ROS in SSCs. We observed that the basal level of ROS was significantly higher in *Pgc1a^{-/-}* SSCs than in WT SSCs, as determined by MitoTracker red staining. Furthermore, while ROS production was induced by tumor necrosis factor (TNF) in WT SSCs, it was significantly greater in *Pgc1a^{-/-}* SSCs after TNF treatment (Figure S7A). Furthermore, depletion of *PGC-1a^{-/-}* in SSCs significantly reduced the induction of negative regulators of ROS, including *Ucp2* and Catalase (Figure S7B).

We further screened downstream key transcription factors associated with SSC differentiation. Intriguingly, we found that the depletion of PGC-1 α in SSCs significantly inhibited the induction of the transcriptional coactivator with a PDZ-binding domain (TAZ) during osteogenic differentiation, as determined by western blot analysis (Figure 7A). TAZ is a key transcription co-activator in the Hippo signaling pathway and has been identified as an important switch of SSC fate decisions (Hong et al., 2005; Park et al., 2015). TAZ can function as a co-activator of RUNX2 to promote osteogenic differentiation while inhibiting adipogenesis as a co-repressor of PPAR γ . Very recently, it has been shown that the deletion of TAZ using Osterix-cre partially reduced bone formation (Kegelman et al., 2018). qRT-

PCR further confirmed that loss of PGC-1 α significantly reduced basal and induced levels of TAZ in SSCs (Figure 7B). Further, in human SSCs, induction of TAZ was also inhibited by siRNA knockdown of PGC-1 α (Figure S7D). Of note, another downstream effector of the Hippo pathway, YAP, was not affected by PGC-1 α depletion (Figures 7A and S7C). During adipogenic differentiation, loss of PGC-1 α also markedly suppressed TAZ expression (Figure 7C).

To test whether TAZ mediated the effect of PGC-1 α on SSC differentiation, we restored TAZ expression in *Pgc1a*^{-/-} SSCs using lentiviruses expressing TAZ (Figure S7E). The restoration of TAZ expression significantly enhanced osteogenic differentiation *Pgc1a*^{-/-} SSCs, as evidenced by ALP (Figures 7D and S7F) and Alizarin red staining (ARS) (Figures 7E and S7G). In addition, restoration of TAZ expression also abolished the enhancement of adipogenic differentiation in *Pgc1a*^{-/-} SSCs (Figure 7F).

We next investigated the molecular mechanism by which PGC-1 α transcriptionally controlled TAZ expression. Nuclear respiratory factor-2 (NRF2), an Ets family transcription factor, is a known co-activator of PGC-1 α in mitochondrial biogenesis, and mounting oxidative stress can disable the ability of NRF2 to bind with DNA (Gleyzer et al., 2005). Interestingly, we found that three Ets binding sites (GGAAG; 44 to 48 bp, 664 to 668 bp, and 914 to 918 bp) exist within 1 kb upstream of the transcription start sites (TSSs) at the *Taz* promoter. To test whether PGC-1 α and NRF2 could directly regulate *Taz* expression, we performed chromatin immunoprecipitation (ChIP) assays on *Pgc1a*^{+/+} and *Pgc1a*^{-/-} SSCs after 0 and 12 hr of osteogenic induction (OI). While OI significantly enhanced binding of PGC-1 α and NRF2 to the *Taz* promoter in *Pgc1a*^{+/+} SSCs, these inductions were significantly lost in *Pgc1a*^{-/-} SSCs (Figure 7G). The expression of NRF2 was not affected by the PGC-1 α depletion in SSCs (Figure S7H), therefore the loss of PGC-1 α likely reduced recruitment of NRF2 to the *Taz* promoter. We also found potential NRF1 and ERR α binding sites in the promoter of *Taz*. However, the ChIP assay did not reveal significant binding of NRF1 or ERR α at the *Taz* promoter upon osteogenic induction (Figures S7I and S7J).

TAZ is a Runx2 coactivator for the *Bglap* gene, a late marker gene of osteoblast differentiation (Hong et al., 2005). As TAZ expression was inhibited by loss of PGC-1 α , binding of TAZ at *Bglap* promoter was significantly inhibited (Figure 7H). While the basal level of PGC-1 α on the *Taz* promoter in *Pgc1a*^{-/-} SSCs was abolished, the recruitment of PGC-1 α to the *Taz* promoter was not significantly induced in SSCs during adipogenic induction. Moreover, there was no significant change in NRF2 occupancy on the *Taz* promoter (Figure 7I).

We found significantly lower levels of *Taz*, but not *Yap* mRNA, in femoral bone cells of 3-month-old *Pgc1a*^{-/-} mice compared to WT mice (Figure 7J). To further confirm that PGC-1 α promoted bone formation through TAZ, we also examined whether gain- or loss-of-function of PGC-1 α affected TAZ expression *in vivo*. IHC of aged bone marrow further showed that TAZ expression was lower in *Pgc1a*^{-/-} compared to *Pgc1a*^{+/+} mice (Figures 7K and S7K), which was confirmed by IF (Figure S7L). Interestingly, we observed a modest increase in TAZ expression in bone marrow cells, including osteoblasts lining on trabecular

bone surfaces in *LepR;Pgc1a^{w/w}* mice upon OVX, probably due to increasing bone-formation activity. On the other hand, TAZ was very weakly detected in *LepR;Pgc1a^{f/f}* mice (Figures 7L and S7M), which was also confirmed by IF (Figure S7N). Similar trends were observed in *Prx1;Pgc1a^{f/f}* and *Prx1;Pgc1a^{w/w}* mice (Figures S7O and S7P). Furthermore, we found that PGC-1 α induction enhanced TAZ expression in *rtTA;tetO-Pgc1a* mice compared to wt;tetO-*Pgc1a* mice (Figures 7M and S7Q), as verified by IF (Figure S7R).

DISCUSSION

Our results demonstrate that PGC-1 α plays a critical role in SSC fate decisions and the inhibition of MAT accumulation in osteoporosis and skeletal aging. Several recent studies have focused on the local effects of endocrinal signals on bone-fat switches in adult bone marrow. LepR signaling reportedly promotes adipogenesis and reduces osteogenesis in high-fat-diet-induced bone-fat imbalance (Yue et al., 2016). Mice with conditional deletion of parathyroid hormone receptor in SSCs had decreased bone mass and increased MAT accumulation (Fan et al., 2017). We found that PGC-1 α expression decreased with age in mice. Importantly, PGC-1 α was also significantly reduced in SSCs from older compared to younger human subjects. *Prx1cre* drives expression in mesenchymal progenitors in the embryonic and adult stages, while *LepRcre* mainly targets adult stem cells in the bone marrow. Utilizing two different cre-lox systems, we showed that loss of PGC-1 α in SSCs plays an important role in the bone-fat imbalance associated with osteoporosis. However, it should be mentioned that the relationship between bone formation and MAT accumulation in the bone marrow is not always mutually exclusive. For instance, MAT increases along with high cortical bone mass in rosiglitazone-induced models in C3H/HeJ mice (Ackert-Bicknell et al., 2009; Fazeli et al., 2013). In the future, it will be interesting to elucidate the underlying mechanism of this correlation.

Our *in vitro gain-* and loss-of-function studies further confirmed that PGC-1 α intrinsically restrains adipocyte differentiation in the bone marrow. On the contrary, previous studies showed that PGC-1 α depletion did not affect brown fat differentiation but significantly impaired thermogenic gene induction (Uldry et al., 2006). Meanwhile, PGC-1 α reportedly serves as a critical transcriptional co-activator for the beige to brown fat switch, where binding of PGC-1 α to the PRDM16/CtBP complex favors transcription of brown fat genes (Kajimura et al., 2008). Recent studies demonstrated that bone MAT is different from both white and brown adipose tissues (Hardouin et al., 2016; Krings et al., 2012) and can function as an endocrine organ to produce adiponectin (Cawthorn et al., 2014). The molecular mechanisms that control adipogenesis might be different in the bone marrow than in other regions. Our findings further lend support to the notion that MAT is distinct from brown and white fat. Interestingly, we found that the depletion of PGC-1 α in osteoblasts did not affect MAT accumulation, further confirming that PGC-1 α regulates adipogenesis in SSCs. However, loss of PGC-1 α in osteoblasts also impaired bone formation in osteoporosis, probably because PGC-1 α is an important metabolic factor. Our findings from *2.3crePgc1a^{f/f}* mice confirmed that PGC-1 α contributes to the functions of mature osteoblasts in addition to playing a role in cell lineage specification. However, staining of proliferative and apoptotic adipocytes appears to rule out the likelihood that PGC-1 α controls the expansion and maintenance of osteoblasts and adipocytes.

The bone-fat imbalance in aging and osteoporosis is associated with an increasingly pro-inflammatory tissue environment with mounting oxidative stress (Yu and Wang, 2016). Consistent with its reported role in regulating antioxidant enzymes, our finding that loss of PGC-1 α impairs the defense against ROS could provide a novel link between cell fate determination and oxidative stress in osteoporosis. It is well known that the loss of PGC-1 α promotes inflammation by activating NF- κ B (Handschin and Spiegelman, 2008). NF- κ B-mediated inflammation has often been linked to oxidative stress (Almeida et al., 2011; Kim et al., 2010; Lee et al., 2005). Our results suggest that loss of PGC-1 α might be responsible for chronic inflammation and oxidative stress in osteoporosis and skeletal aging (Chang et al., 2009, 2013; Yu et al., 2014). Inflammation and ROS have been shown to promote adipocyte differentiation and are associated with obesity (Catrysse and van Loo, 2017; Ye and Gimble, 2011). Taken together, our findings could point to a potential connection between PGC-1 α and inflammation-driven dysregulation of SSC fate decisions in osteoporotic and aging bone. Our conditional knockout mice indicate that deletion of PGC-1 α in SSCs might indirectly promote osteoclastogenesis and bone resorption by increasing the expression of pro-inflammatory cytokines. The close homolog of PGC-1 α , PGC-1 β , coordinates iron uptake in mitochondrial biogenesis and osteoclast activation (Ishii et al., 2009). Deletion of PGC-1 β in bone marrow macrophages blocks osteoclastogenesis *in vitro* and *in vivo* (Wei et al., 2010). However, the role of PGC-1 α in osteoclastogenesis is not very clear. The alleviation of OVX-induced bone loss following PGC-1 α induction could be partly attributed to a suppression of osteoclastic resorption, and this intriguing phenomenon warrants closer examination by conditional deletion of PGC-1 α in osteoclast precursors.

TAZ has been established as a key SSC fate determinant factor (Hong et al., 2005), but so far, the upstream regulation of TAZ expression has mostly been associated with mechanosensing via extracellular matrix (Dupont et al., 2011). Our studies found that PGC-1 α as a metabolic factor also plays a critical role in the transactivation of TAZ expression in bone cells. Loss of PGC-1 α not only enhances ROS production in SSCs but also significantly impairs TAZ expression both *in vitro* and *in vivo*. This is consistent with reports that increasing ROS could inhibit DNA binding ability of NRF2 (Wu et al., 2013). Paradoxically, it has been reported that ROS could stabilize and activate TAZ expression by cysteine S-glutathionylation in HEK293T cells and kidney tissues (Gandhirajan et al., 2016), but it is possible that the regulation of TAZ by oxidative stress may be cell-context dependent. Moreover, PGC-1 α expression was not impaired in that study. Although the loss of PGC-1 α in SSCs might increase the production of ROS and the presence of ROS could potentially stabilize TAZ, TAZ could not be transcriptionally activated in PGC-1 α -deficient SSCs. Therefore, TAZ expression remained low in PGC-1 α -deficient SSCs. Finally, our gain- and loss-of-function studies *in vivo* confirmed that PGC-1 α is required for TAZ expression in bone tissues. PGC-1 α , a key player in metabolism and antioxidative defense, could serve an osteoprotective role to promote osteogenesis and attenuate adipogenesis. Our findings establish the induction of PGC-1 α as a promising potential therapeutic approach to the treatment of osteoporosis and the prevention of skeletal aging.

STAR★METHODS

CONTACT FOR REAGENT AND RESOURCE SHARING

Further information and requests for reagents may be directed to, and will be fulfilled by the Lead Contact, Dr. Cun-Yu Wang (cwang@dentistry.ucla.edu).

EXPERIMENTAL MODEL AND SUBJECT DETAILS

Mice—All mice used in the study were housed under standard conditions in the animal facility of UCLA. All procedures were performed based on the UCLA Animal Research Committee-approved protocols. *Ppargc1a*^{-/-} (B6.129X1-*Ppargc1a*^{tm1Dpk}/J; Strain origin: C57BL6J/129X1; Cat# JAX:009662); *Ppargc1a*^{fl/fl} (B6N.129(FVB)-*Ppargc1a*^{tm2.1Brsp}/J; Strain origin: C57BL6N/129; Cat# JAX:009666); *tetO-Ppargc1a* (FVB-*Tg(tetO-Ppargc1a)1Dpk*/J; Strain origin: FVB; Cat# JAX:012387); *rtTA* (B6.129S4-*Gt(ROSA)26Sor*^{tm1Sor}/J; C57BL6J/129; Cat# JAX:003309); *LeprCre* (B6.129(Cg)-*Lepr*^{tm2.1cre}*Rck*/J; C57BL6J/129; JAX:008320); and *Prx1Cre* (B6.Cg-*Tg(Prx1-cre)1Cjt*/J; Strain: C57BL/6JxSJL/J; Cat# JAX:005584) mice were purchased from Jackson Laboratory. The mice were purchased as mating pairs, and did not introduce additional genetic background during the mating process. Due to the variety of strains, we used littermate controls for each of the following comparisons: WT versus *Ppargc1a*^{-/-}, *Prx1Cre*; *Ppargc1a*^{w/w} versus *Prx1Cre*; *Ppargc1a*^{fl/fl}; *LepRCre*; *Ppargc1a*^{w/w} versus *LeprCre*; *Ppargc1a*^{fl/fl}; *2.3Colcre*; *Ppargc1a*^{w/w} versus *2.3Colcre*; *Ppargc1a*^{fl/fl}; wt;*tetO-pgc1a* versus *rtTA*;*tetO-pgc1a*. When littermates were not possible, age-matched litters from another dam of the same strain were used in its place. We chose a sample size of at least 8 mice per group based on our previous experience and publications. For *in vivo* studies, animals were randomly divided into different groups and animal experiments were not performed in a blinded fashion. The animal experiments were performed twice independently. For statistical analysis, all animals from each group were pooled together to acquire enough sample size as our statistician advised. All OVX mice were female while WT versus *Ppargc1a*^{-/-} mice in aging study were mixed genders.

Human subjects—Human bone marrow samples were collected from patients admitted to the orthopedic surgery department at Xiangya Hospital of the Central South University in China. All subjects included in the study suffered from femoral head/neck/shaft fractures. Bone marrow was aspirated during bone fracture surgery and joint replacement. The use of human bone marrow samples for this study was approved by the Ethics Committee of Xiangya Hospital of Central South University, and written informed consent was obtained from all participants prior to bone marrow aspiration. The demographic information of patients included is as follows: 23 male patients in 20–40 years of age; 31 male patients in 70–90 years of age; 18 female patients in 20–40 years of age; and 24 female patients in 70–90 years of age. All subjects were screened based on review of medical history and were enrolled based on the exclusion criteria associated with pre-existing conditions affecting the bone metabolism. Specifically, patients were excluded if they had received treatment with glucocorticoids, estrogens, thyroid hormone, parathyroid hormone, fluoride, bisphosphonate, calcitonin, thiazide diuretics, barbiturates, or antiseizure medication.

METHOD DETAILS

OVX, μ CT, and bone histomorphometry—3-month-old female wild-type (WT) and *Ppargc1a*^{-/-} mice were subjected to OVX or sham operation under isoflurane anesthesia. The mice were euthanized 1 month after surgery, except for 2.3cre;*Pgc1^{ff}* and 2.3cre;*Pgc^{w/w}* mice which were euthanized 6 weeks after surgery. For tetO-Pgc1 α mice, 2 mg/ml doxycycline was added to the drinking water to induce the expression of PGC-1 α for four weeks immediately after the surgery. Ten days before euthanasia, mice received intraperitoneal injections of first dose of calcein (0.5 mg/mouse, Sigma-Aldrich). Second calcein injection was given (0.5 mg/mouse, Sigma-Aldrich) three days before euthanasia. Following euthanasia, right femurs were fixed in 70% ethanol for 48 hr and embedded in methyl methacrylate. 8 μ m longitudinal sections were either stained with Toluidine blue for osteoblast count or examined under a fluorescent microscope to evaluate MAR, MS/BS and BFR as described previously (Chang et al., 2009). Of note, in cases where the fluorescent mineralizing front is fuzzy or wide, the midline is taken to calculate the distance between fronts.

Left femurs were fixed in 10% formaldehyde for μ CT scanning. The specimens were fitted in a cylindrical sample holder (20.5 mm in diameter) with the long axis of the femur perpendicular to the X-ray source. Specimens were scanned with a Scanco μ CT40 scanner (Scanco Medical) set to 55kVp and 70 μ A at 8 μ m resolution. The bone volume (mm³), BMD, Tb.N, and Tb.Sp in the region of interest were measured directly with μ CT Evaluation Program V4.4A (Scanco Medical). We defined the regions of interest as the areas between 0.3 mm and 0.6 mm proximal to the growth plate in the distal femurs, in order to include the secondary trabecular spongiosa. A threshold of 250 was used for evaluation of all scans. For visualization, the segmented data was imported and reconstructed as a 3D-image displayed in μ CT Ray V3.0 (Scanco Medical). For cortical bone analysis, the tibiae specimens were scanned similarly. 1mm thick sections immediately distal to the tibiofibular junction were used as the region of interest. Cortical thickness was calculated directly from the Scanco μ CT Evaluation Program. For histomorphometric analysis, 3 random fields of view per sample/mouse were randomly taken, imaged with an Olympus-IX51 inverted microscope with CellSens software. Osteoblast number (Ob.N) were counted along the trabecular bone surface under 20X magnification, and osteoblast surface (Ob.S) was measured as the length of lining surface divided by bone surface (BS), calculated using SPOT5.3 Microscopy Imaging Software. Osteoclast parameters were similarly analyzed following TRAP staining. Adipocyte numbers and area per tissue area were analyzed on H&E staining images using the same software.

IHC and IF—After scanning, the specimens were decalcified in 5% EDTA, embedded in paraffin, sectioned into 5 μ m-thick slices and stained as previously described. For IHC, manufacturer's instruction from a HRP-DAB Cell and Tissue Staining kit was used (R&D Systems). Antibodies used include rabbit polyclonal anti-FABP4 (ab13979, 1:200, Abcam), rabbit polyclonal anti-TAZ (NB110-58359, 1:200, Novus Biologicals), rabbit polyclonal anti-NF- κ B p65 NLS specific (600-401-127, 1:200, Rockland) and rabbit polyclonal antiPGC-1 α (ab54481; 1:100, Abcam). For IF, sections were permeabilized in PBS containing 0.1% Triton X-100, followed by blocking in 1% BSA in PBST for 30 minutes.

Primary antibodies include rabbit monoclonal anti-Ki67 (RM-9016, 1:200, Thermo Fisher), rabbit monoclonal anti-cleaved caspase-3 (9661S, 1:100, Cell Signaling), goat polyclonal anti-osteocalcin (C42094, 1:100, LifeSpan BioSci), and mouse monoclonal anti-Perilipin (AM09128, 1:100, OriGene). After incubation with primary antibodies overnight, sections were washed in PBS and incubated with appropriate secondary antibodies with Cy2 or Cy3 (1:100; Jackson ImmunoResearch). Sections were sealed with SlowFade Mountant with DAPI.

For quantification of Integral Optical Density in IHC and IF, ImagePro Plus (Ver 6.0.0.260, Media Cybernetics) was used following a previously described protocol (Yu et al., 2014). Three random fields of view per sample/mouse were randomly taken for each specimen, and the average values were taken as the data point for each specimen.

μ CT analysis of marrow adipose tissue (MAT)—Tibiae were harvested with muscle carefully removed and fixed in 10% buffered formalin for 24 hours. Bones were decalcified in EDTA for 2 weeks, and cut off just proximal to the ankle joint. Glass vials containing 1:1 ratio of 2% osmium tetroxide and 5% potassium dichromate solution were used to immerse the tibiae to stain the marrow adipose tissue for 2 days in room temperature. μ CT scanning was conducted with Scanco μ CT40 at 55kVp and 70 μ A at 16 mm resolution. For analysis of marrow adipose tissue, BV/TV was measured in the proximal 3 mm of the tibiae in order to include medullary canals containing the rMAT; as well as in cMAT in the end of tibiae distal to the tibiofibular joint (Scheller et al., 2015).

Tissue RNA isolation and serum analysis—For tissue collection for RT-PCR to assess PGC-1 α expression, we extracted specific fresh mouse tissues and crushed them while frozen in liquid nitrogen. Tissue homogenate was created by sonication before subsequent protein/RNA isolation. For bone marrow specifically, freshly isolated bone marrow from mouse femur was subjected to Red Blood Cell lysis buffer (Sigma Aldrich) to remove red blood cells. Human BMSCs were purchased from ATCC.

We also collected blood samples from the heart during euthanasia and isolated serum for serology. For *2.3crePgc1a^{ff}*, *2.3crePgc1a^{w/w}*, rTA;tetO-*Pgc1a* and wt;tetO-*Pgc1a* mice, we initially used traditional 1.5 mL Eppendorf tubes for blood collection, allowing the clot to form on ice for 1 hour before centrifuging to obtain the serum. For the rest of the mouse strains and experiments, we improved our serum collection by using BD® Microtainer tubes which contained a clot activator and gel barrier for serum collection. Serum ELISA was performed with an OCN ELISA kit (LifeSpan Biosciences), TRAP5b ELISA kit (Sigma) and IL-6 ELISA kit (R&D system) based on manufacturer's instructions.

SSC isolation and flow cytometry—For mouse SSC isolation, bone marrow from WT and knockout mice was flushed out using a 25 gauge needle. Briefly, cells were digested with trypsin for 2min at 37°C, and passed through a 40 μ m strainer. Cell were cultured in alpha modified Eagle's medium supplemented with 10% fetal bovine serum (FBS) supplemented with 200 μ M L-glutamine and non-essential amino acids for 2 weeks. Colony forming cells were harvested and washed twice with FACS buffer (PBS, 10mM EDTA, 2% FBS), resuspended and stained with anti-CD11b-FITC (1:100 BioLegend Cat#101205) anti-

CD29-PE (1:100, Biolegend Cat#102207), anti-CD45-PerCP (1:100, Biolegend Cat#103129) and anti-Sca1-APC (1:100, BioLegend Cat#108111) for 30min on ice. Sca1⁺CD29⁺CD45⁻CD11b⁻ SSCs were sorted by fluorescence-activated cell sorting (FACS) as described previously (Chang et al., 2013). Cell gating was based on comparison with isotype controls and single stained controls.

For human bone marrow SSC isolation, human bone marrow cells were incubated with anti-STRO-1-FITC (1:100, BioLegend Cat#340106), anti-CD45-APC (1:100, BioLegend Cat#304012;), and anti-CD146-PE (1:100, BioLegend Cat#361008) at 4°C for 30 minutes. Acquisition of CD146⁺STRO-1⁺CD45⁻ cells was performed on a FACS Aria model (BD Biosciences).

Cell differentiation and viral transduction—SSCs were cultured in alpha modified Eagle's medium supplemented with 10% fetal bovine serum (FBS) supplemented with 200 μM L-glutamine and non-essential amino acids. To induce osteogenic differentiation, we used mineralization-inducing media containing 100 μM/ml ascorbic acid, 2 mM β-glycerophosphate, and 10 nM dexamethasone. ALP activity assay and Alizarin Red staining were performed as described previously (Yu et al., 2014). To induce adipogenic differentiation, we cultured SSCs in adipogenic-inducing media containing 0.5 mM isobutylmethylxanthine, 0.5 μM hydrocortisone, and 60 μM indomethacin (Sigma-Aldrich). Media were changed every 3 days. After 3 weeks of culture *in vitro*, Oil-Red-O staining was performed to detect the lipid droplets using an Oil-red-O staining kit according to the manufacturer's instruction (Diagnostic Biosystems). For BMMΦs, marrow cells were cultured in DMEM with 10% FBS, and stimulated with M-CSF (100ng/ml) for 3 days.

For viral transduction, adenoviruses were generated by co-transfection of pAd-Track-Flag-HA-PGC-1α (Addgene) with packaging plasmids into HEK293T cells as described previously (Ding et al., 2013). pAd-Track-CMV was used as negative control (Addgene). SSCs were infected with viruses for 24 hours before proceeding to induction for osteogenic/adipogenic differentiation. Similarly, lentiviruses overexpressing Flag-tagged TAZ were packaged in 293T cells using pLenti-EF-FH-TAZ-ires-blast plasmids (Addgene).

Western Blotting—Cells were lysed in RIPA buffer (10 mM Tris-HCL, 1 mM EDTA, 1% sodium dodecyl sulfate [SDS], 1% Nonidet P-40, 1: 100 proteinase inhibitor cocktail, 50 mM β-glycerophosphate, 50 mM sodium fluoride). The samples were separated on a 10% SDS-PAGE gel and transferred to PVDF membranes by a semi-dry transfer apparatus (Bio-Rad). After blotting with 5% non-fat milk for 1 hour, the membranes were incubated with primary antibodies at 4°C overnight (Abcam Cat#ab54481, 1:1000 for anti-PGC-1α; Santa Cruz Cat#sc21382, 1:1000 for anti-NRF2; Novus Biologicals Cat#NB110-58359, 1:1000 for anti-TAZ; Sigma-Aldrich, Cat#T9026, 1:10000 for α-tubulin). The immunocomplexes were incubated with horseradish peroxidase-conjugated anti-rabbit or antimouse IgG (Promega) and detected with SuperSignal reagents (Pierce) as previously described (Chang et al., 2009). For

Cell Stem Cell 23, 193–209.e1–e5, August 2, 2018 e4 quantification of western blots, band intensities for each antibody-specific blots were measured as areas under the intensity profile

curve, using the ImageJ software. Relative band intensity for each lane was calculated after normalization against intensity for α -tubulin in the corresponding lane.

Mitotracker staining—To measure ROS production, SSCs were seeded in a 12-well plate (0.5×10^5 cells/well). When the cell density reached ~60% confluence, cells were serum-starved for 4 h and then treated with TNF (5 ng/ml). The cells were stained with Mitotracker Red (Molecular Probes) for 30 min in a 37°C humidified incubator containing 5% CO₂ and stored in the dark until analysis. The sections were imaged with an Olympus IX-51 inverted microscope and the CellSens software.

qRT-PCR—For qRT-PCR, total RNA was extracted using TRIzol reagent (Thermo Fisher Scientific Cat#15596026), and 1 μ g of RNA was used for the RT reaction with random primer (Thermo Fisher Scientific Cat#48190011), dNTP mix (Thermo Fisher Scientific Cat#18427013), and M-MuLV Reverse Transcriptase (New England Biolabs Cat#M0253L). Quantification of mRNA was determined by real-time PCR using a SYBRGreen supermix (Bio-Rad Cat#1708880). Relative expression levels of the indicated genes were compared with GAPDH expression. Primer sequences are listed in Table S1.

Chromatin Immunoprecipitation (ChIP) Assay—Cells were rinsed with PBS and incubated with a dimethyl 3,3' dithiobispropionimidate-HCl (DTBP) (Pierce) solution (5 mmol) for 10 min at room temperature, followed by cross-linking via 1% formaldehyde for 30 min in a 37°C water-bath. The amount of total DNA was normalized across the samples. 1ml of diluted immunocomplexes were incubated at 4°C overnight with polyclonal antiPGC-1 α (1.5 μ g, Abcam Cat#ab54481), polyclonal anti-NRF2 (2 μ g, Santa Cruz Cat#sc-28312), polyclonal anti-NRF1 (2 μ g, Abcam Cat#ab34682), polyclonal anti-ERR α (2 μ g, Millipore Cat#07-662) or anti-rabbit IgG (negative control). The samples were incubated with Fastflow Protein G agarose beads for 1 hour and beads were washed with high and low salt solutions to remove unspecific binding. The immunocomplexes were then eluted from the beads and reverse cross-linked overnight at 65°C. Immunoprecipitated DNA was isolated using the DNA Clean and Concentrator kit (Zymo Research). The precipitated DNA samples were quantified using Realtime PCR. Primer sequences are listed in Table S1. Data are presented as the percentage of input DNA.

STATISTICAL ANALYSIS

Numerical data and histograms were expressed as the mean \pm sd. Two-tailed Student's t test was performed between two groups and a difference was considered statistically significant with $p < 0.05$. For comparison between groups involving two genotypes of mice along with Sham and OVX procedures or aging conditions, the differences were assessed using two-way ANOVA with HolmSidak posthoc test. For multiple comparisons such as mRNA gene expression in Figure 4, one-way ANOVA was used. $p < 0.05$ was considered significant.

Supplementary Material

Refer to Web version on PubMed Central for supplementary material.

ACKNOWLEDGMENTS

This work was supported by the National Institute of Dental and Craniofacial Research (grants R01DE024828 and R01DE019412), the National Institute of Arthritis and Musculoskeletal and Skin Diseases (grant R01AR063089), and the National Center for Advancing Translational Sciences (grant KL2TR001882).

REFERENCES

- Ackert-Bicknell CL, Shockley KR, Horton LG, Lecka-Czernik B, Churchill GA, and Rosen CJ (2009). Strain-specific effects of rosiglitazone on bone mass, body composition, and serum insulin-like growth factor-I. *Endocrinology* 150, 1330–1340. [PubMed: 18948404]
- Almeida M, Han L, Ambrogini E, Weinstein RS, and Manolagas SC (2011). Glucocorticoids and tumor necrosis factor α increase oxidative stress and suppress Wnt protein signaling in osteoblasts. *J. Biol. Chem* 286, 44326–44335. [PubMed: 22030390]
- Ambrosi TH, Scialdone A, Graja A, Gohlke S, Jank AM, Bocian C, Woelk L, Fan H, Logan DW, Schürmann A, et al. (2017). Adipocyte accumulation in the bone marrow during obesity and aging impairs stem cell-based hematopoietic and bone regeneration. *Cell Stem Cell* 20, 771–784.e6. [PubMed: 28330582]
- Arany Z, He H, Lin J, Hoyer K, Handschin C, Toka O, Ahmad F, Matsui T, Chin S, Wu PH, et al. (2005). Transcriptional coactivator PGC-1 α controls the energy state and contractile function of cardiac muscle. *Cell Metab.* 1, 259–271. [PubMed: 16054070]
- Balaban RS, Nemoto S, and Finkel T (2005). Mitochondria, oxidants, and aging. *Cell* 120, 483–495. [PubMed: 15734681]
- Bianco P, and Robey PG (2015). Skeletal stem cells. *Development* 142, 1023–1027. [PubMed: 25758217]
- Bianco P, Cao X, Frenette PS, Mao JJ, Robey PG, Simmons PJ, and Wang C-Y (2013). The meaning, the sense and the significance: translating the science of mesenchymal stem cells into medicine. *Nat. Med* 19, 35–42. [PubMed: 23296015]
- Catrysse L, and van Loo G (2017). Inflammation and the metabolic syndrome: the tissue-specific functions of NF- κ B. *Trends Cell Biol.* 27, 417–429. [PubMed: 28237661]
- Cawthorn WP, Scheller EL, Learman BS, Parlee SD, Simon BR, Mori H, Ning X, Bree AJ, Schell B, Broome DT, et al. (2014). Bone marrow adipose tissue is an endocrine organ that contributes to increased circulating adiponectin during caloric restriction. *Cell Metab.* 20, 368–375. [PubMed: 24998914]
- Chang J, Wang Z, Tang E, Fan Z, McCauley L, Franceschi R, Guan K, Krebsbach PH, and Wang CY (2009). Inhibition of osteoblastic bone formation by nuclear factor-kappaB. *Nat. Med* 15, 682–689. [PubMed: 19448637]
- Chang J, Liu F, Lee M, Wu B, Ting K, Zara JN, Soo C, Al Hezaimi K, Zou W, Chen X, et al. (2013). NF- κ B inhibits osteogenic differentiation of mesenchymal stem cells by promoting β -catenin degradation. *Proc. Natl. Acad. Sci. USA* 110, 9469–9474. [PubMed: 23690607]
- Devlin MJ, and Rosen CJ (2015). The bone-fat interface: basic and clinical implications of marrow adiposity. *Lancet Diabetes Endocrinol.* 3, 141–147. [PubMed: 24731667]
- Ding X, Pan H, Li J, Zhong Q, Chen X, Dry SM, and Wang CY (2013). Epigenetic activation of P1 promotes squamous cell carcinoma metastasis. *Sci. Signal* 6, 1–13.
- Dupont S, Morsut L, Aragona M, Enzo E, Giulitti S, Cordenonsi M, Zanconato F, Le Dıgabel J, Forcato M, Bicciato S, et al. (2011). Role of YAP/TAZ in mechanotransduction. *Nature* 474, 179–183. [PubMed: 21654799]
- Fan Y, Hanai JI, Le PT, Bi R, Maridas D, DeMambro V, Figueroa CA, Kir S, Zhou X, Mannstadt M, et al. (2017). Parathyroid hormone directs bone marrow mesenchymal cell fate. *Cell Metab.* 25, 661–672. [PubMed: 28162969]
- Farmer SR (2006). Transcriptional control of adipocyte formation. *Cell Metab.* 4, 263–273. [PubMed: 17011499]

- Fazeli PK, Horowitz MC, MacDougald OA, Scheller EL, Rodeheffer MS, Rosen CJ, and Klibanski A (2013). Marrow fat and bone—new perspectives. *J. Clin. Endocrinol. Metab* 98, 935–945. [PubMed: 23393168]
- Gandhirajan RK, Jain M, Walla B, Johnsen M, Bartram MP, Huynh Anh M, Rinschen MM, Benzing T, and Schermer B (2016). Cysteine S-glutathionylation promotes stability and activation of the Hippo downstream effector transcriptional co-activator with PDZ-binding motif (TAZ). *J. Biol. Chem* 291, 11596–11607. [PubMed: 27048650]
- Gill JF, Santos G, Schnyder S, and Handschin C (2018). PGC-1 α affects aging-related changes in muscle and motor function by modulating specific exercise-mediated changes in old mice. *Aging Cell* 17, e12697.
- Gleyzer N, Vercauteren K, and Scarpulla RC (2005). Control of mitochondrial transcription specificity factors (TFB1M and TFB2M) by nuclear respiratory factors (NRF-1 and NRF-2) and PGC-1 family coactivators. *Mol. Cell. Biol* 25, 1354–1366. [PubMed: 15684387]
- Gregoire FM, Smas CM, and Sul HS (1998). Understanding adipocyte differentiation. *Physiol. Rev* 78, 783–809. [PubMed: 9674695]
- Gregory CA, Ylostalo J, and Prockop DJ (2005). Adult bone marrow stem/ progenitor cells (MSCs) are preconditioned by microenvironmental “niches” in culture: a two-stage hypothesis for regulation of MSC fate. *Sci. STKE* 2005, pe37–pe37. [PubMed: 16046665]
- Handschin C, and Spiegelman BM (2008). The role of exercise and PGC1 α in inflammation and chronic disease. *Nature* 454, 463–469. [PubMed: 18650917]
- Hardouin P, Rharass T, and Lucas S (2016). Bone marrow adipose tissue: to be or not to be a typical adipose tissue? *Front. Endocrinol. (Lausanne)* 7, 85. [PubMed: 27445987]
- Hong JH, Hwang ES, McManus MT, Amsterdam A, Tian Y, Kalmukova R, Mueller E, Benjamin T, Spiegelman BM, Sharp PA, et al. (2005). TAZ, a transcriptional modulator of mesenchymal stem cell differentiation. *Science* 309, 1074–1078. [PubMed: 16099986]
- Ishii KA, Fumoto T, Iwai K, Takeshita S, Ito M, Shimohata N, Aburatani H, Taketani S, Lelliott CJ, Vidal-Puig A, and Ikeda K (2009). Coordination of PGC-1 β and iron uptake in mitochondrial biogenesis and osteoclast activation. *Nat. Med* 15, 259–266. [PubMed: 19252502]
- Justesen J, Mosekilde L, Holmes M, Stenderup K, Gasser J, Mullins JJ, Seckl JR, and Kassem M (2004). Mice deficient in 11 β -hydroxysteroid dehydrogenase type 1 lack bone marrow adipocytes, but maintain normal bone formation. *Endocrinology* 145, 1916–1925. [PubMed: 14715714]
- Kajimura S, Seale P, Tomaru T, Erdjument-Bromage H, Cooper MP, Ruas JL, Chin S, Tempst P, Lazar MA, and Spiegelman BM (2008). Regulation of the brown and white fat gene programs through a PRDM16/ CtBP transcriptional complex. *Genes Dev.* 22, 1397–1409. [PubMed: 18483224]
- Kalajzic I, Staal A, Yang W-P, Wu Y, Johnson SE, Feyen JHM, Krueger W, Maye P, Yu F, Zhao Y, et al. (2005). Expression profile of osteoblast lineage at defined stages of differentiation. *J. Biol. Chem* 280, 24618–24626. [PubMed: 15834136]
- Kawai M, and Rosen CJ (2010). PPAR γ : a circadian transcription factor in adipogenesis and osteogenesis. *Nat. Rev. Endocrinol* 6, 629–636. [PubMed: 20820194]
- Kegelman CD, Mason DE, Dawahare JH, Horan DJ, Vigil GD, Howard SS, Robling AG, Bellido TM, and Boerckel JD (2018). Skeletal cell YAP and TAZ combinatorially promote bone development. *FASEB J.* 32, 2706–2721. [PubMed: 29401582]
- Kfoury Y, and Scadden DT (2015). Mesenchymal cell contributions to the stem cell niche. *Cell Stem Cell* 16, 239–253. [PubMed: 25748931]
- Kim MS, Yang Y-M, Son A, Tian YS, Lee S-I, Kang SW, Muallem S, and Shin DM (2010). RANKL-mediated reactive oxygen species pathway that induces long lasting Ca²⁺ oscillations essential for osteoclastogenesis. *J. Biol. Chem* 285, 6913–6921. [PubMed: 20048168]
- Krings A, Rahman S, Huang S, Lu Y, Czernik PJ, and Lecka-Czernik B (2012). Bone marrow fat has brown adipose tissue characteristics, which are attenuated with aging and diabetes. *Bone* 50, 546–552. [PubMed: 21723971]
- Lee NK, Choi YG, Baik JY, Han SY, Jeong DW, Bae YS, Kim N, and Lee SY (2005). A crucial role for reactive oxygen species in RANKL-induced osteoclast differentiation. *Blood* 106, 852–859. [PubMed: 15817678]

- Li H, Liu P, Xu S, Li Y, Dekker JD, Li B, Fan Y, Zhang Z, Hong Y, Yang G, et al. (2017). FOXPI controls mesenchymal stem cell commitment and senescence during skeletal aging. *J. Clin. Invest* 127, 1241–1253. [PubMed: 28240601]
- Lin J, Handschin C, and Spiegelman BM (2005). Metabolic control through the PGC-1 family of transcription coactivators. *Cell Metab.* 1, 361–370. [PubMed: 16054085]
- Logan M, Martin JF, Nagy A, Lobe C, Olson EN, and Tabin CJ (2002). Expression of Cre Recombinase in the developing mouse limb bud driven by a Prxl enhancer. *Genesis* 33, 77–80. [PubMed: 12112875]
- Manolagas SC (2010). From estrogen-centric to aging and oxidative stress: a revised perspective of the pathogenesis of osteoporosis. *Endocr. Rev* 31, 266–300. [PubMed: 20051526]
- McCauley LK (2010). c-Maf and you won't see fat. *J. Clin. Invest* 120, 3440–3442. [PubMed: 20877008]
- Park HW, Kim YC, Yu B, Moroishi T, Mo JS, Plouffe SW, Meng Z, Lin KC, Yu FX, Alexander CM, et al. (2015). Alternative Wnt signaling activates YAP/TAZ. *Cell* 162, 780–794. [PubMed: 26276632]
- Puigserver P, Wu Z, Park CW, Graves R, Wright M, and Spiegelman BM (1998). A cold-inducible coactivator of nuclear receptors linked to adaptive thermogenesis. *Cell* 92, 829–839. [PubMed: 9529258]
- Russell LK, Mansfield CM, Lehman JJ, Kovacs A, Courtois M, Saffitz JE, Medeiros DM, Valencik ML, McDonald JA, and Kelly DP (2004). Cardiac-specific induction of the transcriptional coactivator peroxisome proliferator-activated receptor γ coactivator-1 α promotes mitochondrial biogenesis and reversible cardiomyopathy in a developmental stage-dependent manner. *Circ. Res* 94, 525–533. [PubMed: 14726475]
- Scheller EL, Doucette CR, Learman BS, Cawthorn WP, Khandaker S, Schell B, Wu B, Ding S-Y, Bredella MA, Fazeli PK, et al. (2015). Regionspecific variation in the properties of skeletal adipocytes reveals regulated and constitutive marrow adipose tissues. *Nat. Commun* 6, 7808. [PubMed: 26245716]
- Schwartz AV (2015). Marrow fat and bone: review of clinical findings. *Front. Endocrinol. (Lausanne)* 6, 40. [PubMed: 25870585]
- St-Pierre J, Drori S, Uldry M, Silvaggi JM, Rhee J, Jäger S, Handschin C, Zheng K, Lin J, Yang W, et al. (2006). Suppression of reactive oxygen species and neurodegeneration by the PGC-1 transcriptional coactivators. *Cell* 127, 397–408. [PubMed: 17055439]
- Uldry M, Yang W, St-Pierre J, Lin J, Seale P, and Spiegelman BM (2006). Complementary action of the PGC-1 coactivators in mitochondrial biogenesis and brown fat differentiation. *Cell Metab.* 3, 333–341. [PubMed: 16679291]
- Wang W, Li C, Pang L, Shi C, Guo F, Chen A, Cao X, and Wan M (2014). Mesenchymal stem cells recruited by active TGF β contribute to osteogenic vascular calcification. *Stem Cells Dev.* 23, 1392–1404. [PubMed: 24512598]
- Wei W, Wang X, Yang M, Smith LC, Dechow PC, Sonoda J, Evans RM, and Wan Y (2010). PGC1beta mediates PPARgamma activation of osteoclastogenesis and rosiglitazone-induced bone loss. *Cell Metab.* 11, 503–516. [PubMed: 20519122]
- Wilson C (2014). Bone: oxidative stress and osteoporosis. *Nat. Rev. Endocrinol* 10, 3.
- Wu H, Xiao Y, Zhang S, Ji S, Wei L, Fan F, Geng J, Tian J, Sun X, Qin F, et al. (2013). The Ets transcription factor GABP is a component of the hippo pathway essential for growth and antioxidant defense. *Cell Rep.* 3, 1663–1677. [PubMed: 23684612]
- Xiong J, Onal M, Jilka RL, Weinstein RS, Manolagas SC, and O'Brien CA (2011). Matrix-embedded cells control osteoclast formation. *Nat. Med* 17, 1235–1241. [PubMed: 21909103]
- Ye J, and Gimble JM (2011). Regulation of stem cell differentiation in adipose tissue by chronic inflammation. *Clin. Exp. Pharmacol. Physiol* 38, 872–878. [PubMed: 21883381]
- Ye L, Fan Z, Yu B, Chang J, Al Hezaimi K, Zhou X, Park N-H, and Wang C-Y (2012). Histone demethylases KDM4B and KDM6B promotes osteogenic differentiation of human MSCs. *Cell Stem Cell* 11, 50–61. [PubMed: 22770241]
- Yu B, and Wang CY (2016). Osteoporosis: the result of an 'aged' bone microenvironment. *Trends Mol. Med.* 22, 641–644. [PubMed: 27354328]

- Yu B, Chang J, Liu Y, Li J, Kevork K, Al-Hezaimi K, Graves DT, Park NH, and Wang CY (2014). Wnt4 signaling prevents skeletal aging and inflammation by inhibiting nuclear factor- κ B. *Nat. Med* 20, 1009–1017. [PubMed: 25108526]
- Yue R, Zhou BO, Shimada IS, Zhao Z, and Morrison SJ (2016). Leptin receptor promotes adipogenesis and reduces osteogenesis by regulating mesenchymal stromal cells in adult bone marrow. *Cell Stem Cell* 18, 782–796. [PubMed: 27053299]
- Zaidi M, Buettner C, Sun L, and Iqbal J (2012). Minireview: The link between fat and bone: does mass beget mass? *Endocrinology* 153, 2070–2075. [PubMed: 22467495]
- Zhou BO, Yue R, Murphy MM, Peyer JG, and Morrison SJ (2014). Leptin-receptor-expressing mesenchymal stromal cells represent the main source of bone formed by adult bone marrow. *Cell Stem Cell* 15, 154–168. [PubMed: 24953181]

Highlights

- Loss of PGC-1 α in SSCs is associated with osteoporosis and skeletal aging
- Loss of PGC-1 α promotes adipogenesis of SSCs at the expense of osteogenesis
- PGC-1 α induction prevents MAT accumulation and bone loss in osteoporosis
- PGC-1 α controls bone-fat balance by inducing TAZ

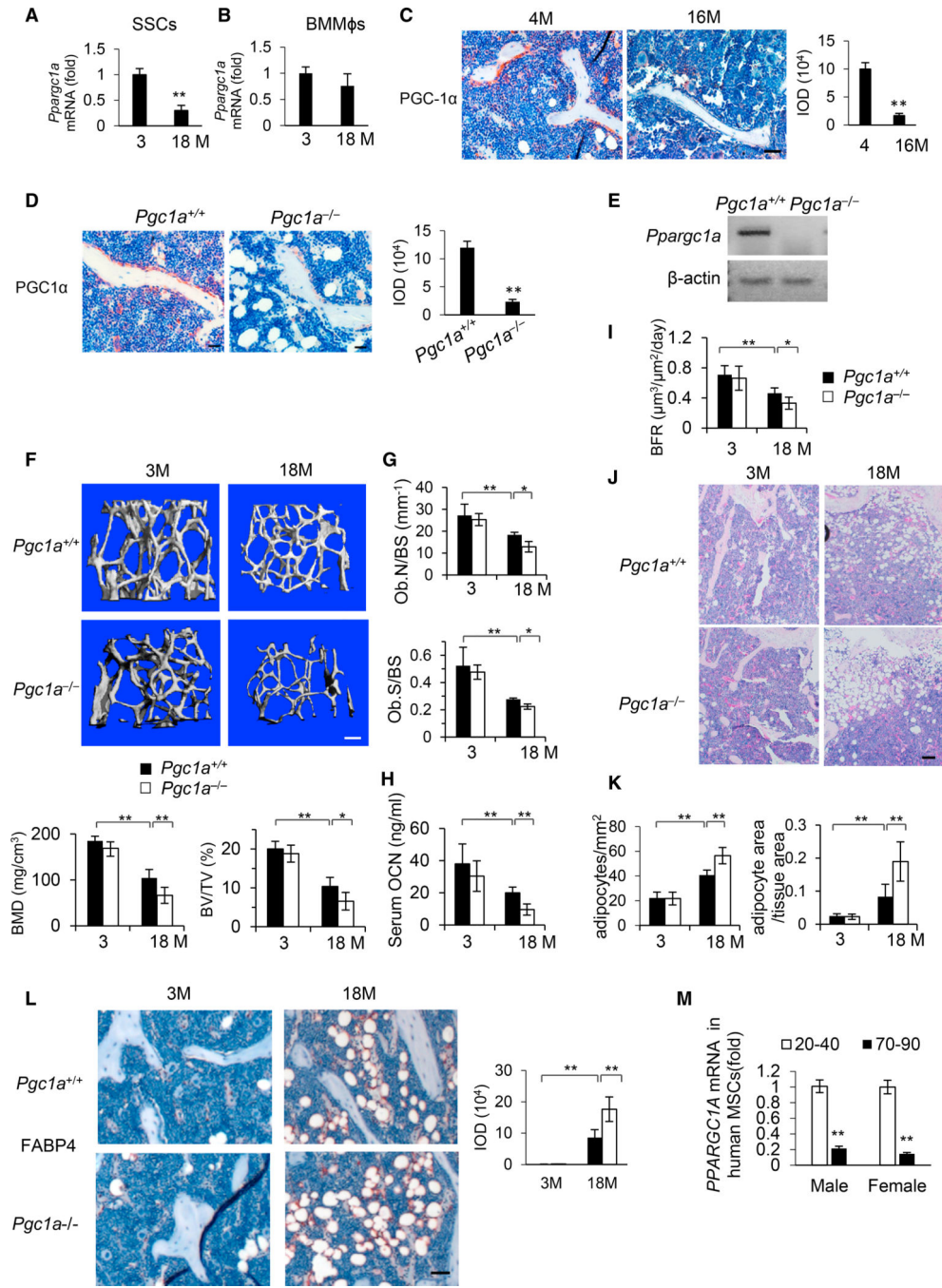


Figure 1. Loss of PGC-1α Potentiated Bone Loss and MAT Accumulation in Skeletal Aging
 (A) mRNA expression of *Ppargc1a* from bone marrow SSCs of 3- and 18-month-old mice, as determined by qRT-PCR. **p* < 0.05; ***p* < 0.01 by Student's *t* test.
 (B) mRNA expression of *Ppargc1a* from marrow monocytes and/or macrophages of 3- and 18-month-old mice, as determined by qRT-PCR. **p* < 0.05; ***p* < 0.01 by Student's *t* test.
 (C) IHC of PGC-1α in femurs of 4- and 16-month-old mice and IOD quantification. Scale bars, 50 μm.

(D) IHC of PGC-1 α in *Pgc1a*^{+/+} and *Pgc1a*^{-/-} mouse bone marrow and IOD quantification. Scale bar, 50 μ m.

(E) Expression of *Ppargc1a* in bone marrow homogenates of *Pgc1a*^{+/+} and *Pgc1a*^{-/-} mice was determined by RT-PCR.

(F) Quantitative measurements of BMD and BV/TV of femurs from 3- and 18-month-old *Pgc1a*^{+/+} and *Pgc1a*^{-/-} mice by μ CT. Scale bar, 0.3 mm.

(G) Osteoblast number (Ob.N/BS) and osteoblast surface (Ob.S/BS) in young and aged *Pgc1a*^{+/+} and *Pgc1a*^{-/-} mice.

(H) ELISA of serum OCN in 3- and 18-month-old *Pgc1a*^{+/+} and *Pgc1a*^{-/-} mice.

(I) Bone formation rate (BFR) of 3- and 18-month-old *Pgc1a*^{+/+} and *Pgc1a*^{-/-} mice as determined by dual labeling.

(J) Representative H&E staining of 3- and 18-month-old mouse femurs.

(K) Adipocyte number per tissue area and area of adipocytes per tissue area measured based on H&E images.

(L) Representative IHC of FABP4 and IOD quantification. Scale bar, 80 μ m.

(M) *PPARGC1A* mRNA expression of SSCs isolated from human bone marrow ($n > 13$ subjects per group) of two age groups.

All data are presented as means \pm SD. ** $p < 0.01$ by two-way ANOVA with Holm-Sidak post hoc test. For (G)–(L), $n = 8$ mice per group. See also Figure S1.

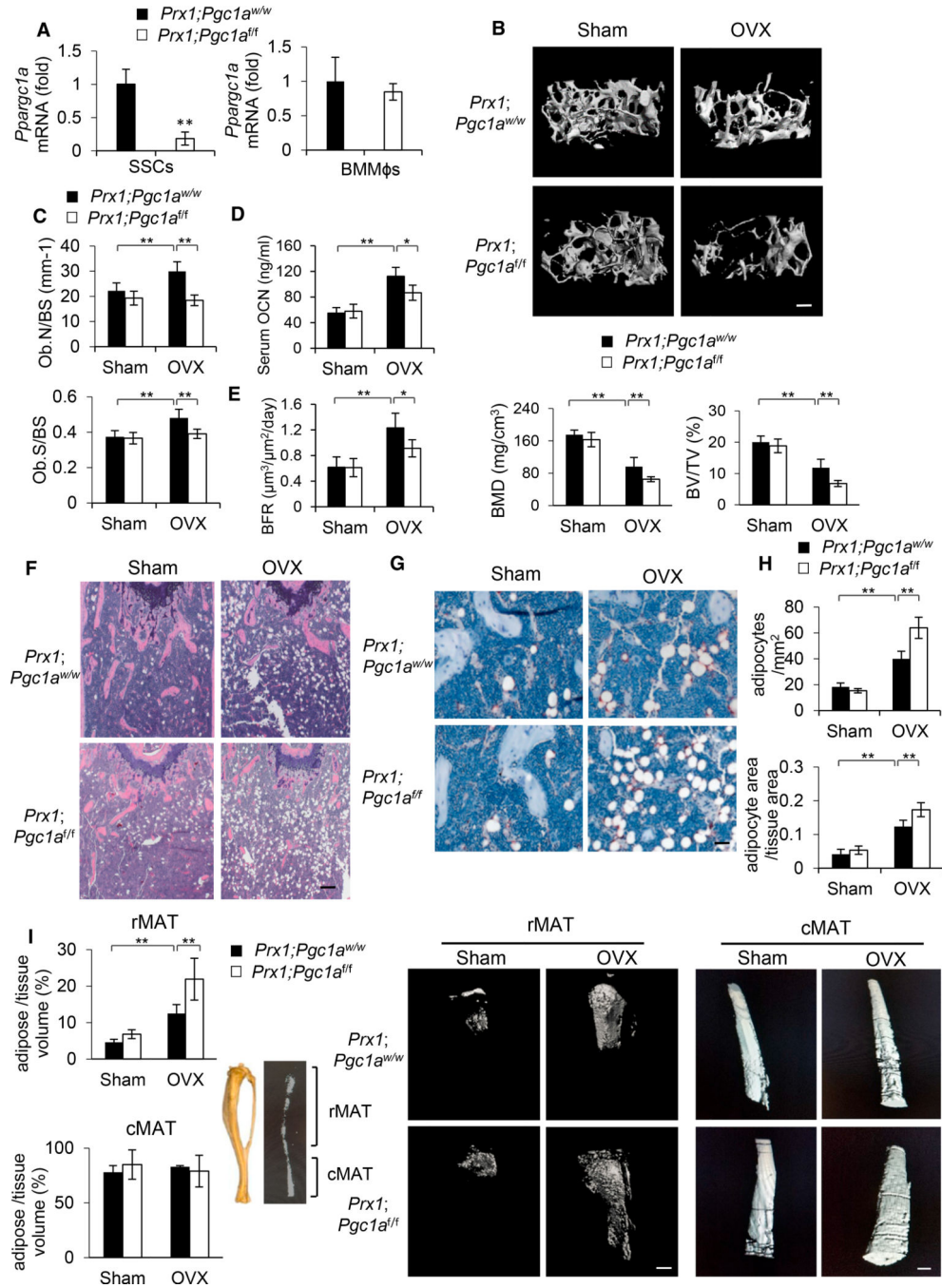


Figure 2. Depletion of PGC-1α in Mesenchymal Cells using Prx1-cre Exacerbated Bone-Fat Imbalance in OVX-Induced Osteoporosis

(A) *Ppargc1a* mRNA in $Sca1^{+}CD29^{+}CD45^{-}CD11b^{-}$ SSCs (left) and bone marrow monocytes and/or macrophages (BMMΦs, right) from 2-month-old *Prx1;Pgc1a^{fl/fl}* and *Prx1;Pgc1a^{w/w}* mice was assessed by qRT-PCR.

(B) Quantitative measurements of BMD and BV/TV of femurs from *Prx1;Pgc1a^{fl/fl}* and *Prx1;Pgc1a^{w/w}* mice following sham and OVX by μCT. Scale bar, 0.3 mm.

(C) Osteoblast number (Ob.N/BS) and osteoblast surface (Ob.S/BS) in *Prx1;Pgc1a^{fl/fl}* and *Prx1;Pgc1a^{w/w}* mice.

- (D) Serum OCN levels in *Prx1;Pgc1a^{f/f}* and *Prx1;Pgc1a^{w/w}* mice.
- (E) BFR of *Prx1;Pgc^{f/f}* and *Prx1;Pgc^{w/w}* mice after OVX.
- (F) Representative H&E staining images of *Prx1;Pgc1a^{f/f}* and *Prx1;Pgc1a^{w/w}* mouse femurs.
- (G) Representative immunostaining of FABP4. Scale bar, 80 μ m.
- (H) Adipocyte number per tissue area and area of adipocytes per tissue area measured based on H&E images.
- (I) Quantitative measurements of adipocyte volume and representative μ CT images of rMAT in the proximal tibiae and cMAT in the distal tibiae (n = 6 mice per group). Scale bar, 0.3 mm.
- *p < 0.05; **p < 0.01 by two-way ANOVA with Holm-Sidak post hoc test. For (B)–(I), n = 8 mice per group. Also see Figure S2.

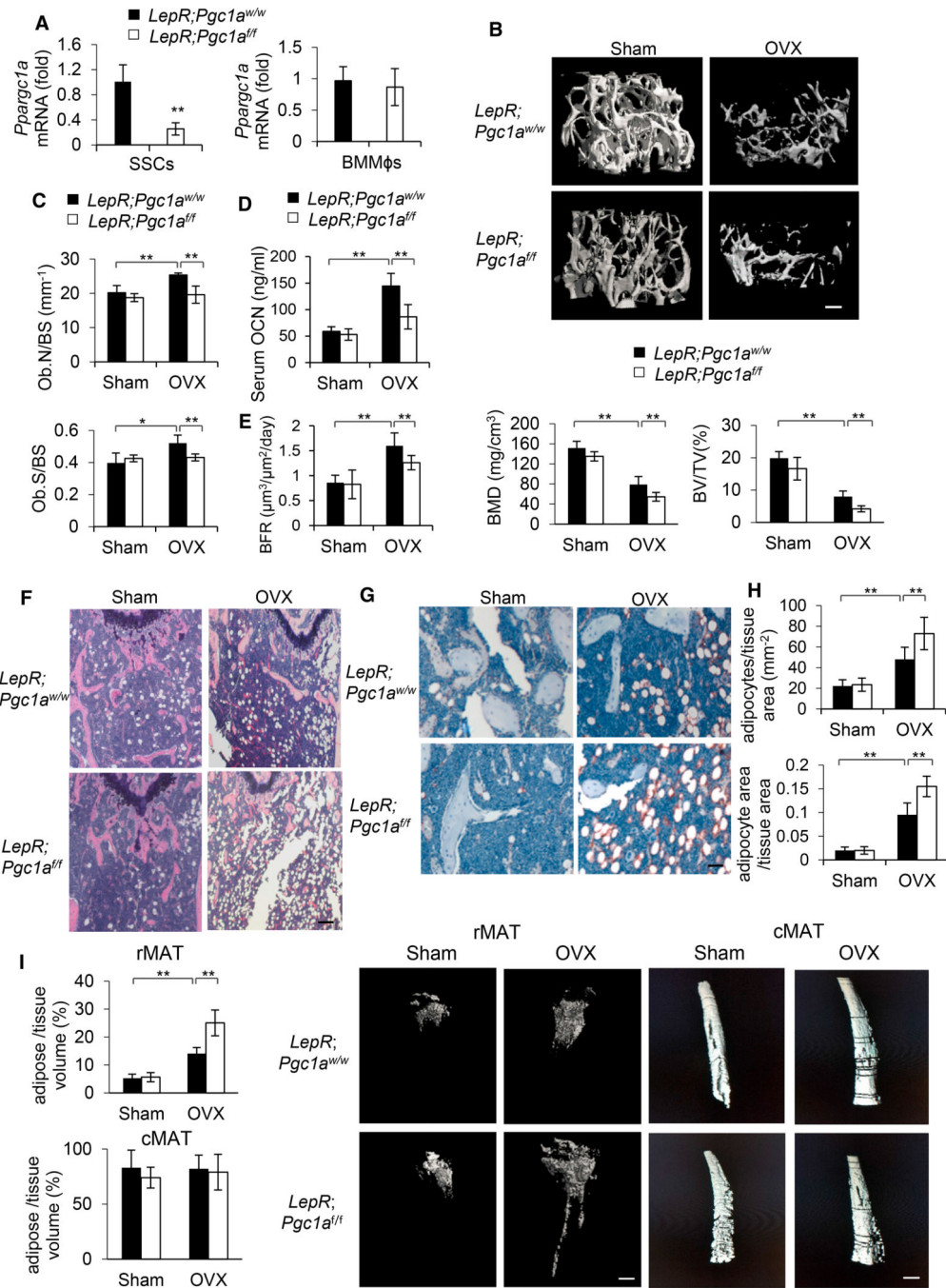


Figure 3. Depletion of PGC-1α in Mesenchymal Cells using LepR-cre Exacerbated Bone-Fat Imbalance in OVX-Induced Osteoporosis
 (A) *Ppargc1a* mRNA in *Sca1*⁺*CD29*⁺*CD45*⁻*CD11b*⁻ SSCs (left) and BMMFφs (right) from 2-month-old *LepR;Pgc1a*^{f/f} and *LepR;Pgc1a*^{w/w} mice was assessed via qRT-PCR (left).
 (B) Representative μCT images of femurs from *LepR;Pgc1a*^{f/f} and *LepR;Pgc1a*^{w/w} mice following sham and OVX. Scale bar, 0.3 mm. Quantitative measurements of BMD and BV/TV by μCT.
 (C) Osteoblast number (Ob.N/BS) and osteoblast surface (Ob.S/BS) in *LepR;Pgc1a*^{f/f} and *LepR;Pgc1a*^{w/w} mice.

- (D) BFR of *LepR;Pgc1a^{f/f}* and *LepR;Pgc1a^{w/w}* mice.
- (E) Serum OCN level in *LepR;Pgc1a^{f/f}* and *LepR;Pgc1a^{w/w}* mice.
- (F) Representative H&E staining images of *LepR;Pgc1a^{f/f}* and *LepR;Pgc1a^{w/w}* mouse femurs.
- (G) Representative IHC of FABP4. Scale bar, 80 μ m.
- (H) Adipocyte number per tissue area and area of adipocytes per tissue area measured based on H&E images.
- (I) Quantitative measurements of adipocyte volume and representative μ CT images of rMAT and cMAT in tibiae of *LepR;Pgc1a^{f/f}* and *LepR;Pgc1a^{w/w}* mice following sham and OVX (n = 6 mice per group). Scale bar, 0.3 mm.
- All data are presented as means \pm SD. *p < 0.05; **p < 0.01 by two-way ANOVA with Holm-Sidak post hoc test. For (B)–(I), n = 8 mice per group. See also Figure S3.

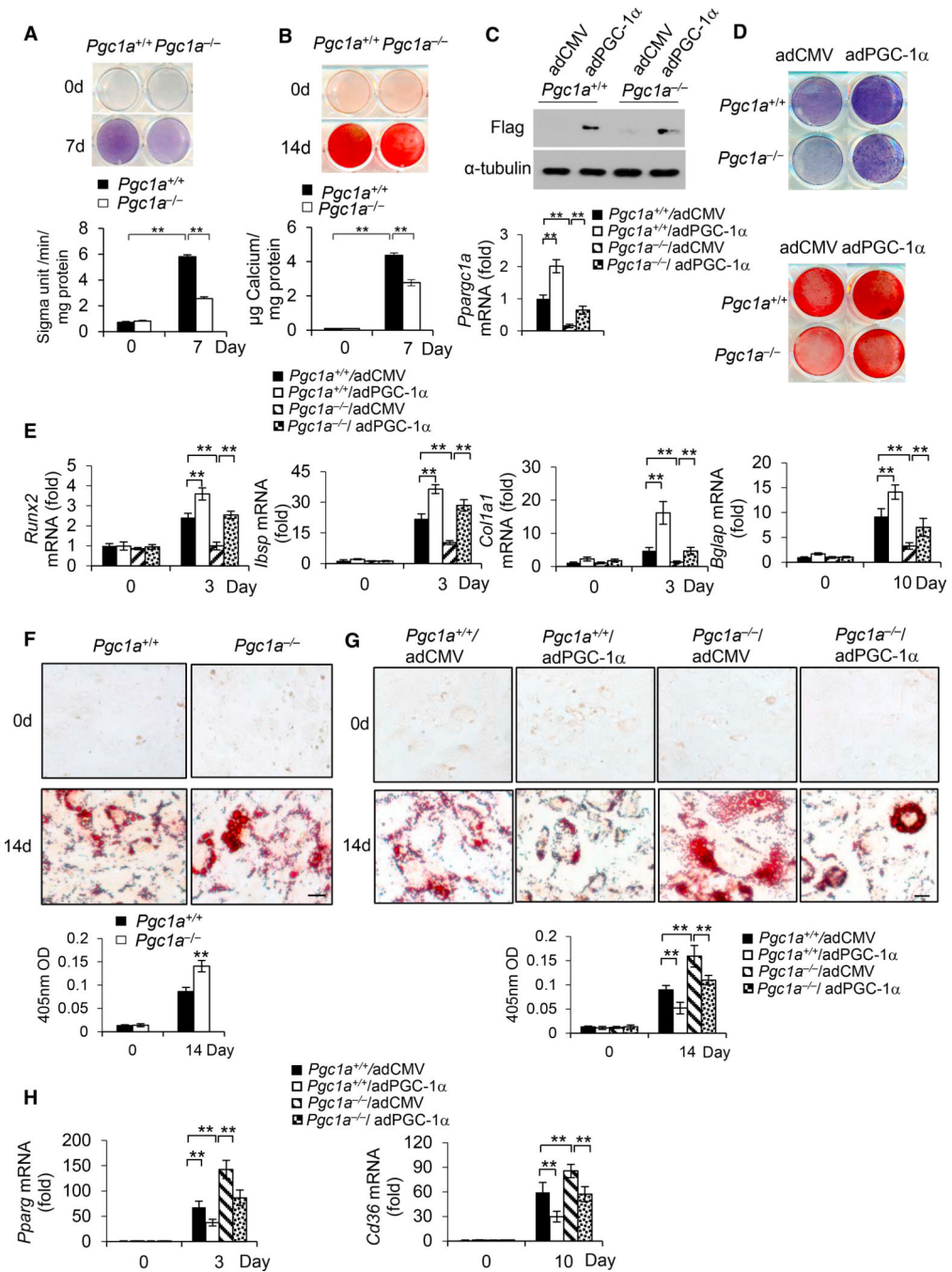


Figure 4. PGC-1α Controls Osteoblastic and Adipogenic Differentiation of SSCs In Vitro

(A) Osteoblastic differentiation of SSCs isolated from *Pgc1a*^{+/+} and *Pgc1a*^{-/-} mouse bone marrow was determined by ALP staining.
 (B) Mineralized nodule formation of SSCs from *Pgc1a*^{+/+} and *Pgc1a*^{-/-} mice was assessed by alizarin red staining.
 (C) Adenovirus expressing FLAG-tagged PGC-1α (adPGC-1α) or control CMV (adCMV) was transfected to overexpress PGC-1α in *Pgc1a*^{+/+} (WT) and *Pgc1a*^{-/-} (KO) SSCs. Top

panel shows western blot confirming overexpression. Bottom panel shows mRNA expression of *Ppargc1a* in SSCs, as assessed using qRT-PCR.

(D) Restoration of PGC-1 α in *Pgc1a*^{-/-} SSCs restored osteogenic differentiation, as determined by ALP and ARS staining.

(E) qRT-PCR showing that restoration of PGC- α 1 in *Pgc1a*^{-/-} SSCs restored the expression of the key osteogenic marker genes, including *Runx2*, *Ibsp*, *Colla1*, and *Bglap*.

(F) Oil red O staining of *Pgc1a*^{+/+} and *Pgc1a*^{-/-} SSCs after 14 days of adipogenic induction.

(G) The restoration of PGC-1 α in *Pgc1a*^{-/-} SSCs inhibited adipogenic differentiation as determined by oil red O staining.

(H) qRT-PCR showing that restoration of PGC-1 α in *Pgc1a*^{-/-} SSCs inhibited the expression of the key adipogenic marker genes *Pparg* and *Cd36*.

All experiments were repeated three times, and a representative dataset is presented. All data are presented as means \pm SD. *p < 0.05; **p < 0.01 by Student's t test for (A and B) and one-way ANOVA for (C and E-H). See also Figure S4.

(E) ELISA of serum OCN in *2.3cre;Pgc1a^{f/f}* and *2.3cre;Pgc1a^{w/w}* mice.

(F) Representative H&E staining in femurs from *2.3cre;Pgc1a^{f/f}* and *2.3cre;Pgc1a^{w/w}* mice.

(G) Adipocyte number per tissue area and area of adipocytes per tissue area in the distal end of femurs. Scale bar, 150 μ m.

(H) Quantitative measurements of adipocyte volume and μ CT images of rMAT and cMAT in tibiae of *2.3cre;Pgc1a^{f/f}* and *2.3cre;Pgc1a^{w/w}* mice (n = 6 mice per group). Scale bar, 0.3 mm. All data are presented as means \pm SD. *p < 0.05; **p < 0.01 by two-way ANOVA with Holm-Sidak post hoc test. For (B)–(G), n = 8 mice per group. Also see Figure S5.

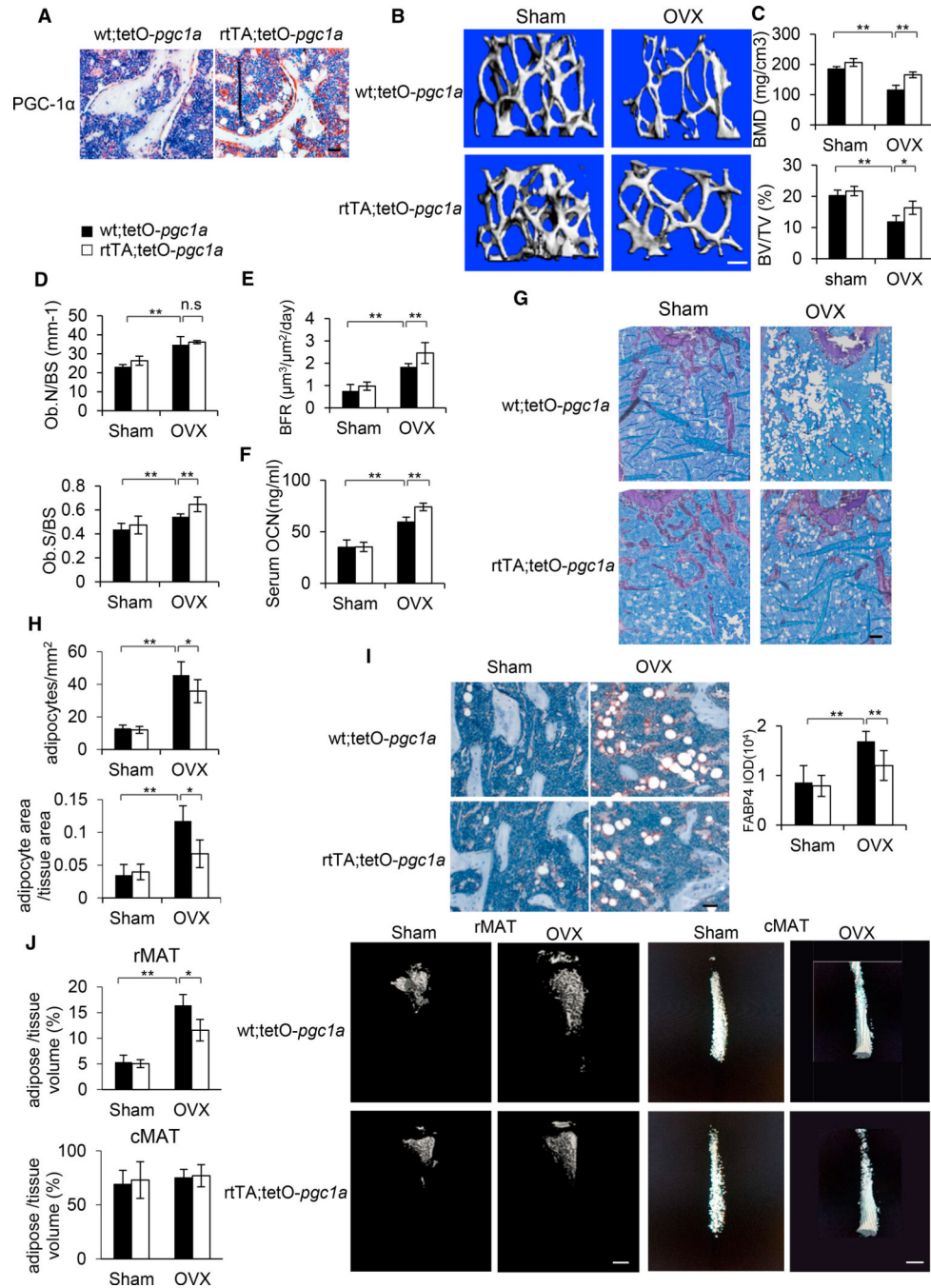


Figure 6. Induction of PGC-1α Mitigates Bone Loss and MAT Accumulation in Osteoporosis
 (A) Immunostaining showing PGC-1α expression in femurs of *wt;tetO-Pgc1a* and *rtTA;tetO-Pgc1a* mice following doxycycline induction. Scale bar, 60 μm.
 (B) Representative μCT images of femurs from *wt;tetO-Pgc1a* and *rtTA;tetO-Pgc1a* mice following doxycycline induction and then OVX or sham operation. Scale bar, 0.3 mm.
 (C) BMD and BV/TV of *wt;tetO-Pgc1a* and *rtTA;tetO-Pgc1a* mice were measured by μCT following doxycycline induction and OVX.

(D) Morphometric measurements of osteoblasts in wt;tetO-*Pgc1a* and rtTA;tetO-*Pgc1a* mice following doxycycline induction and OVX.

(E) BFR of wt;tetO-*Pgc1a* and rtTA;tetO-*Pgc1a* mice.

(F) ELISA of serum OCN in wt;tetO-*Pgc1a* and rtTA;tetO-*Pgc1a* mice.

(G) Representative toluidine blue staining delineating trabecular bone and adipocytes in the distal end of femurs. Scale bar, 150 μ m. (H) Adipocyte number per tissue area and area of adipocytes per tissue area in wt;tetO-*Pgc1a* and rtTA;tetO-*Pgc1a* mice following doxycycline induction and OVX.

(I) Representative IHC of FABP4. Scale bar, 50 μ m.

(J) Quantitative measurements of adipocyte volume and representative mCT images of rMAT and cMAT in the tibiae of wt;tetO-*Pgc1a* and rtTA;tetO-*Pgc1a* mice following sham and OVX (n = 6 mice per group). Scale bar, 0.3 mm.

All data are presented as means \pm SD. *p < 0.05; **p < 0.01. For (C)-(H), n = 8 mice per group. See also Figure S6.

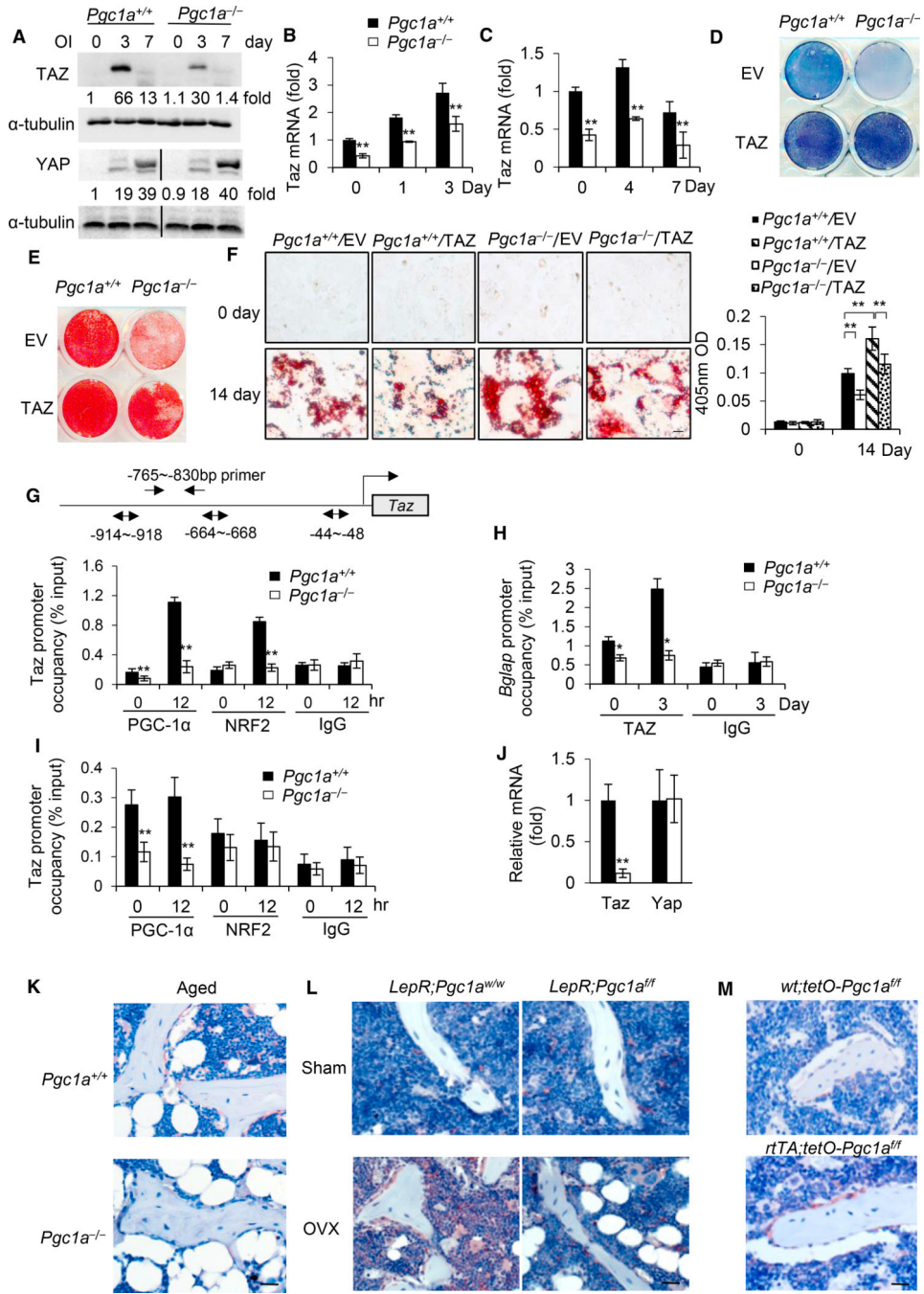


Figure 7. PGC-1α Controls SSC Cell Fate Decisions through TAZ

(A) The expression of TAZ and YAP in *Pgc1a*^{+/+} and *Pgc1a*^{-/-} SSCs was examined by western blot following osteogenic induction. Relative band intensity was normalized against α-tubulin and determined using ImageJ. The YAP image was cropped from two parts of the same blot, with two irrelevant lanes removed.

(B) qRT-PCR showing *Taz* mRNA expression in *Pgc1a*^{+/+} and *Pgc1a*^{-/-} SSCs following osteogenic induction.

- (C) qRT-PCR showing *Taz* mRNA expression in *Pgc1a*^{+/+} and *Pgc1a*^{-/-} SSCs following adipogenic induction.
- (D) Overexpression of TAZ in *Pgc1a*^{+/+} and *Pgc1a*^{-/-} SSCs potentiated osteogenic differentiation, as determined by ALP staining.
- (E) Overexpression of TAZ in *Pgc1a*^{+/+} and *Pgc1a*^{-/-} SSCs potentiated osteogenic differentiation, as determined by alizarin red staining.
- (F) Overexpression of TAZ in *Pgc1a*^{+/+} and *Pgc1a*^{-/-} SSCs inhibited adipogenic differentiation, as determined by oil red O staining.
- (G) ChIP assays showed that PGC-1 α and NRF2 were recruited to the *Taz* promoter following osteogenic induction. Top panel indicates the primer position relative to the three ETS binding sites at the *Taz* promoter.
- (H) ChIP assays showed that TAZ binding to the *Bglap* promoter was induced following osteogenic induction.
- (I) ChIP assays of PGC-1 α and NRF2 on the *Taz* promoter following adipogenic induction.
- (J) mRNA expression of *Taz* and *Yap* in tissue RNA isolated from bone cells in 3-month-old *Pgc1a*^{+/+} and *Pgc1a*^{-/-} mice.
- (K) IHC of TAZ in 18-month-old *Pgc1a*^{+/+} and *Pgc1a*^{-/-} mouse femurs. Scale bar, 150 μ m.
- (L) IHC of TAZ in *LepR;Pgc1a*^{fl/fl} and *LepR;Pgc1a*^{w/w} mice after OVX and sham operations. Scale bar, 150 μ m.
- (M) IHC of TAZ in wt;*tetO-Pgc1a* and *rtTA;tetO-Pgc1a* mice after sham operation. Scale bar, 100 μ m.
- All experiments were repeated three times, and a representative dataset is presented. All data are presented as means \pm SD. *p < 0.05; **p < 0.01 by Student's t test. See also Figure S7.

KEY RESOURCES TABLE

REAGENT or RESOURCE	SOURCE	IDENTIFIER
Antibodies		
Rabbit Polyclonal anti-PGC1 α	Abcam	Cat#ab54481 RRID:AB_881987
Rabbit Polyclonal anti-FABP4	Abcam	Cat#ab13979 RRID:AB_1951817
Rabbit Polyclonal anti-TAZ (WWTR1)	Novus Biologicals	Cat#NB110-58359 RRID:AB_922585
Mouse monoclonal anti-NRF2 (GABP- α)	Santa-Cruz	Cat#sc28312 RRID:AB_627647
Mouse monoclonal anti- α -tubulin	Sigma-Aldrich	Cat#T9026 RRID: AB_477593
Rabbit polyclonal anti-YAP	Santa-Cruz	Cat#sc-15407 RRID: AB_2273277
Rabbit polyclonal anti-IgG(isotype control)	Abcam	Cat#ab27478 RRID: AB_2616600
Rat monoclonal anti-mouse CD11b FITC	BioLegend	Cat#101205 RRID: AB_312788
Rat monoclonal anti-mouse CD29 PE	BioLegend	Cat#102207 RRID: AB_312884
Rat monoclonal anti-mouse CD45 PerCP	Biolegend	Cat#103129 RRID: AB_893343
Rat monoclonal anti-mouse Sca-1 APC	Biolegend	Cat#108111 RRID: AB_313348
Rabbit polyclonal anti-estrogen-related receptor α	Millipore	Cat# 07-662 RRID: AB_11212282
Rabbit polyclonal anti-NRF1	Abcam	Cat#ab34682 RRID: AB_2236220
Rabbit monoclonal anti-Ki67	ThermoFisher	Cat #RM-9106 RRID: AB_2335745
Rabbit monoclonal anti-cleaved Caspase-3	Cell Signaling	Cat#9661S RRID: AB_2341188
Goat polyclonal anti-mouse osteocalcin	LifeSpan BioSci	Cat#LS-C42094 RRID: AB_2065056
Mouse monoclonal anti-Perilipin-1	OriGene Tech.	Cat#AM09128SU RRID: AB_10649872
Rabbit polyclonal anti-NF κ B p65 NLS specific	Rockland	Cat#600-401-271 RRID: AB_2269511
Chemicals, Peptides, and Recombinant Proteins		
MEM α	Thermo Fisher Scientific	Cat#12571063
L-Glutamine (200mM)	Thermo Fisher Scientific	Cat# 25030081
Non-essential amino acid (100X)	Thermo Fisher Scientific	Cat#11140050
dexamethasone	Sigma-Aldrich	Cat#D4902
β -Glycerophosphate	Sigma-Aldrich	Cat#G9422
L-Ascorbic acid	Sigma-Aldrich	Cat#A4403
3-isobutyl-1-methylxanthine	Sigma-Aldrich	Cat#I7018
Indomethacin	Sigma-Aldrich	Cat#I7378
Fetal Bovine Serum	Thermo Fisher Scientific	Cat#10437028
M-MuLV Reverse Transcriptase	New England Biolabs	Cat#M0253L
Random Primers	Thermo Fisher Scientific	Cat#48190011
dNTP	Thermo Fisher Scientific	Cat#18427013
Penicillin-Streptomycin (10,000 U/mL)	Thermo Fisher Scientific	Cat#15140122
Trypsin-EDTA	Thermo Fisher Scientific	Cat#R001100
Lipofectamine RNAiMAX Transfection Reagent	Thermo Fisher Scientific	Cat#13778150
RIPA Buffer	Sigma-Aldrich	Cat#R0278
TRIzol Reagent	Thermo Fisher Scientific	Cat#15596026
Doxycycline hydrochloride	Sigma-Aldrich	Cat#D3447
Democycline hydrochloride	Sigma-Aldrich	Cat#1170000

REAGENT or RESOURCE	SOURCE	IDENTIFIER
Calcein	Sigma-Aldrich	Cat#C0875
Red Blood Cell Lysis Buffer	Sigma-Aldrich	Cat#11814389001
Osmium tetroxide 2% aqueous solution	Polysciences Inc	Cat#23311
Potassium dichromate 5% w/v	Fisher	Cat#SP152-500
Bacterial and Virus Strains		
pLenti-EF-FH-TAZ-ires-blast	Addgene	Cat#52083
pLenti CMV Blast DEST	Addgene	Cat #17451
pAd-Track Flag HA PGC-1 alpha (mouse)	Addgene	Cat#14426
pAd-Track CMV	Addgene	Cat#16405
Critical Commercial Assays		
Oil-Red-O Staining Kit	Diagnostic Biosystems	Cat#KT025
Mouse Osteocalcin (OCN) ELISA kit	LifeSpan Biosciences	Cat#LS-F22474-1
Mouse TRAP5b ELISA kit	Immunodiagnostic systems	Cat#SB-TR103
Mouse IL-6 Quantikine ELISA Kit	R&D systems	Cat#M6000B
MitoTracker Red CMXRos	Molecular Probes/Fisher	Cat#M7512
TRAP staining kit	Sigma-Aldrich	Cat#387A-1KT
SYBR Green Supermix	Bio-Rad	Cat#1708880
Experimental Models: Cell Lines		
Human: bone marrow-derived mesenchymal stem cells	ATCC	PCS-500-012
Experimental Models: Organisms/Strains		
Mouse: Ppargc1a ^{-/-} (B6.129X1-Ppargc1a ^{tm1Dpk/J})	Jackson Laboratory	IMSR_JAX:009662
Mouse: Ppargc1a ^{fl/fl} (B6N.129(FVB)-Ppargc1a ^{tm2.1Brsp/J})	Jackson Laboratory	IMSR_JAX:009666
Mouse: tetO-Ppargc1a (FVB-Tg(tetO-Ppargc1a)1Dpk/J)	Jackson Laboratory	IMSR_JAX:012387
Mouse: rtTA (B6;129S4-Gt(ROSA)26Sor ^{tm1Sor/J})	Jackson Laboratory	IMSR_JAX:003309
Mouse: LeprCre (B6.129(Cg)-Lepr ^{tm2(cre)Rck/J})	Jackson Laboratory	IMSR_JAX:008320
Mouse: Prx1Cre (B6.Cg-Tg(Prrx1-cre)1Cjt/J)	Jackson Laboratory	IMSR_JAX:005584
Oligonucleotides		
siGENOME Human PPARGC1A siRNA	Dharmacon	M-005111-01-0005
Software and Algorithms		
Cellsens	Olympus	http://www.olympus-lifescience.com/en/software/cellsens/
SPOT5.3 Microscopy Imaging Software Advanced	SPOT Imaging	https://webstore.diaginc.com/SPOT-Imaging-Software-For-Microscopy-s/59.htm
μCT Evaluation Program V4.4A and Ray V3.0	Scanco Medical	http://www.scanco.ch/en/systems-solutions/
Image-Pro Plus V6.0.0.260	Media Cybernetics	http://www.mediacy.com/imageproplus
ImageJ V1.46r	NIH	https://imagej.nih.gov/ij/download.html